Original: Submitted: March 19, 2025

Heterogeneous distribution of glial cell marker proteins and of cell nucleus marker in the myelinated region of the normal rat optic nerve

June KAWANO[1,2]

[1]Division of Morphological Sciences, Department of Neurology, Kagoshima University Graduate School of Medical and Dental Sciences, Kagoshima, 890-8544, Japan
[2]Laboratory for Neuroanatomy, Department of Neurology, Kagoshima University Graduate School of Medical and Dental Sciences, Kagoshima, 890-8544, Japan

Running Title: glial cell marker proteins in rat optic nerve (38/45)

*Correspondence to:

June Kawano, M.D., Ph.D.
Division of Morphological Sciences, Department of Neurology,
Kagoshima University Graduate School of Medical and Dental Sciences,
35-1, Sakuragaoka 8-chome, Kagoshima, 890-8544, Japan
E-mail: kawanoj@m2.kufm.kagoshima-u.ac.jp
ORCIDID: 0009-0002-1730-6519

Grant sponsor: Kagoshima University
Grant Number: Annual fund

Main points
- Immunoreactivity of both a glial structure protein, glial fibrillary acidic protein (GFAP), and a glial functional protein, glutamine synthetase, (GS), is strong in the distal (anterior)-most part, but weak in the proximal (posterior) part with a significant decrease in strength along the longitudinal plane of the myelinated region in the normal rat optic nerve.
- Labeling of a cell nucleus marker, bisBenzimide, is also strong in the distal-most part, but weak in the proximal part with a significant decrease in strength along the longitudinal plane of the myelinated region in the normal rat optic nerve.
- Myelin basic protein (MBP)-immunoreactive particles are densely distributed in the distal-most part, however, they are sparsely dispersed in the proximal part with a significant difference in the myelinated region of the normal rat optic nerve.
- The concentrations of GFAP, GS, and of MBP-immunoreactive particles in the distal-most part of the myelinated region suggest that this part is under a mildly pathological condition in the normal rat optic nerve.

KEYWORDS:
Glial fibrillary acidic protein; Glutamine synthetase; Myelin basic protein; Myelin debris-like particles; Normal rat optic nerve; Immunohistochemistry

Abstract

Glial cells are critically important for maintenance of neuronal activity in the optic nerve. The present study documents the distribution of glial structure proteins (GFAP: glial fibrillary acidic protein; MBP: myelin basic protein), a glial functional protein (GS: glutamine synthetase), and of a cell nucleus marker (bisBenzimide) in the various myelinated regions of the normal rat optic nerve. Fourteen optic nerves from 12 male Sprague-Dawley rats were employed. Immunohistochemistry and confocal microscopy were used to investigate the distribution of GFAP, MBP, GS, and of bisBenzimide along the longitudinal plane of the myelinated region. GFAP-immunoreactivity and GS-immunoreactivity were strong in the distal (anterior)-most part, but weak in the proximal (posterior) part with a significant decrease in strength along the longitudinal plane of the myelinated region. bisBenzimide labeling was also strong in the distal-most part, but weak in the proximal part with a significant difference in strength in the myelinated region. MBP-immunoreactive particles and cell nuclei were densely distributed in the distal-most part, however they were sparsely dispersed in the proximal part with a significant difference. The heterogeneous distribution of GFAP, GS, bisBenzimide, cell nuclei, and MBP-immunoreactive particles along the longitudinal plane may be an important functional adaptation that reflects the not uniform nature of the physiological and structural environment of the myelinated region. Notably, the concentrations of GFAP, GS, and of MBP-immunoreactive particles in the distal-most part of the myelinated region suggest that this part is under a mildly pathological condition in the normal rat optic nerve.

(246/250 words)

1 | INTRODUCTION

Glial cells are very important for maintenance of neuronal activity in the optic nerve. The optic nerve is comprised of axons of retinal ganglion cells, interstitial glial cells (astrocytes, oligodendrocytes, neuron glial (NG2) cells, and microglia), and of the fibrovascular septa of the pia mater (Yazdankhah et al., 2021). Glial cells are critically important occupants of the optic nerve that work as a team to maintain its neuronal activity and structural stability. In myelinated region, oligodendrocytes constitute short interfascicular rows of adjacent cells along the length of the optic nerve, which are separated from each other by solitary interfascicular astrocytes. This oligodendrocyte-astrocyte mesh is complemented with regularly spaced NG2 cells and microglia. Oligodendrocytes also constitute the myelin sheaths around axons that facilitate rapid and metabolically efficient conduction of action potentials and are essential for axon integrity and nodal function (Yazdankhah et al., 2021). Astrocytes were originally considered to be passive structural elements, but it is clear now that they are dynamic multifunctional cells that are important for potassium homeostasis, metabolism and axon-glial signaling, as well as the physiology of nodes of Ranvier and contributions to the blood-brain barrier (Khakh and Deneen, 2019; Yazdankhah et al., 2021). In addition to interaction with the axons, glial cells constantly interact with each other, forming a strong and highly efficient network supporting the functionality of the optic nerve. Importantly, since the optic nerve does not contain any synapses, but just axons that extend over the length of the nerve, it has become a popular model to study the interactions of glial cells with axons without having to consider their complex role in maintaining synapse functionality (Yazdankhah et al., 2021).

The optic nerve is essentially a tract in the brain, the fiber of which has no neurolemma, and is enclosed by meninges, which is different from any peripheral nerve (Bron et al., 1997). The axons of retinal ganglion cells are unmyelinated in the retina of the

rat and become myelinated when they leave the eye (Black et al., 1985; Kawano, 2015). The chemoarchitecture of the rodent optic nerve has been investigated by several research groups with focusing on the distributions of astrocytic filaments and myelinated axons (Ffrench-Constant et al., 1988; Morcos and Chan-Ling., 2000; Howell et al., 2007; Kawano et al., 2008; Sun et al., 2009; Balaratnasingam et al., 2014; Kawano, 2015). A very high density of astrocytic filaments has been observed at the junction of the retina and optic nerve. The posterior limit of these astrocytic filaments principally coincides with the beginning of axon myelination (Morcos and Chan-Ling., 2000; Kawano, 2015). Accordingly, the rodent optic nerve has been divided into at least 3 regions: the intra retinal (prelaminar), unmyelinated (laminar, lamina cribrosa, or astrocytic filament dense), and myelinated (retrolaminar, retrobulbar, or astrocytic filament sparse) regions (May, 2003; Morrison et al., 2005; Howell et al., 2007; Kawano et al., 2008; Balaratnasingam et al., 2014; Kawano, 2015).

Until recently, investigations of chemoarchitecture of the rodent optic nerve have been progressed by using immunohistochemistry. In the myelinated region of the normal rodent optic nerve, bundles of myelinated axons have been shown to interdigitate with astrocytes (Morcos and Chan-Ling, 2000; Kawano, 2015). A quantitative study demonstrated that the chemoarchitecture of glial fibrillary acidic protein (GFAP) in the myelinated region is heterogeneously organized: GFAP immunoreactivity is strong in the distal (anterior) region, however, it is moderate in the proximal (posterior) region (Kawano, 2015). As for glutamine synthetase (GS), a quantitative study demonstrated that the chemoarchitecture of GS in the myelinated region is also heterogeneously organized: GS immunoreactivity is moderate in the distal region, however, it is weak in the proximal region. Majority of GS-immunoreactive glial cells are oligodendrocytes in the myelinated region (Kawano, 2015). On the myelinated axon, the nodes of Ranvier are distributed in a regularly spaced manner. Nearly all (>95%) of the nodes contain processes from astrocytes, while fewer than one-half

of nodes are contacted by both the NG2 cell and astrocyte processes in the adult rat optic nerve. Ultrastructural analysis revealed that NG2 cells extend fine finger-like projections that often contact both the nodal axolemma and outermost paranodal myelin loops, while astrocytes extend broader processes covering the entire nodal gap, suggesting different roles of the two glial cell types at the node (Serwanski et al., 2017). In the companion article (Kawano, 2025), we demonstrated distribution of myelin basic protein (MBPh[1])-immunoreactive particles in the distal-most part of the myelinated region of the normal rat optic nerve. We confirmed that MBPh-immunoreaction to these particles was real. In addition, we showed that morphological characteristics of MBPh-immunoreactive particles were similar to those of myelin debris, suggesting that the site of the distribution was under a mildly pathological condition in the normal rat optic nerve (Weinger et al., 2011; Zhou et al., 2019; Wang et al., 2020; Yao et al., 2023; Kawano, 2025). Thus, necessary neuroanatomical facts, demonstrated by using immunohistochemistry in the myelinated region of the rodent optic nerve, have been accumulated. However, information on detailed distribution patterns of glial cell proteins and of glial cell DNA remains limited, especially information on a

[1] In the companion pater (Kawano, 2025), we used two kinds of anti-myelin basic protein (MBP) antibodies which detected different positions of the MBP protein in order to analyze distribution of the MBP protein in the normal rat optic nerve: One was an antibody reacts with Ala-Ser-Asp-Tyr-Lys-Ser (ASDYKS) in position 131-136 of the classic human myelin basic protein (MBPh), another was an antibody reacts with Asp-Glu-Asn-Pro-Val-Val (DENPVV) in position 82-87 of the full length protein of the cow myelin basic protein (MBPc). Here we described not MBP but MBPh to clarify which antibody was used to visualize the MBP protein.

detailed distribution pattern of MBPh-immunoreactive particles. Additionally, shape descriptors of MBPh-immunoreactive particles in each myelinated region remain unknown.

Here we show, by using quantitative immunohistochemical analyses, the concentrations of GFAP, GS, cell nuclei, and of MBPh-immunoreactive particles in the distal-most part of the myelinated region. In addition, we also show that shape descriptors of MBPh-immunoreactive particles are primarily stable from the distal myelinated region through the proximal myelinated region. Finally, based on these facts, we suggest that the site of the concentrations is not under a physiological condition but is under a mildly pathological condition in the normal rat optic nerve, since myelin debris-like MBPh-immunoreactive particles are concentrated on this site (Weinger et al., 2011; Zhou et al., 2019; Wang et al., 2020; Yao et al., 202; Kawano, 2025). In addition, a notion that the site is under the mildly pathological condition is strengthened by two results obtained as follows. The concentration of GFAP in this site suggests astrogliosis, which is a secondary event to damage in the central nervous system (CNS; Messam et al., 2002). A significant increase in GS immunoreactivity of GS-immunoreactive cells in this site indicates a chronic pathological condition (Ben Haim et al., 2021).

2 | MATERIALS AND METHODS

2.1 | Animals and tissue preparation

Male rats (n=12; 12 weeks old; Slc:SD; CLEA Japan, Tokyo, Japan) were deeply anesthetized with sodium pentobarbital (50 mg/kg, i.p.), and perfused transcardially with 4 % paraformaldehyde dissolved in 0.1 M sodium phosphate buffer (PB; pH 7.4) at 4°C. The eyeballs including the optic nerve were removed from the skull, stored in the same fixative for 48 hours, and then immersed in 30 % saccharose in 0.1 M PB at 4°C until they sank. The eyeballs including the optic nerve were frozen in powdered dry ice, and sectioned in the meridian plane at a thickness of 25 μm on a cryostat. Sections were collected in a cryoprotectant medium (Warr et al., 1981; 33.3% saccharose, 1% polyvinylpyrrolidone (K-30), and 33.3% ethylene glycol in 0.067M sodium phosphate buffer (pH 7.4) containing 0.067% sodium azide) and stored at –30 °C prior to use.

All animal experiments were approved by the Institutional Animal Care and Use Committee of Kagoshima University (MD11112; MD15029; MD18058), and were conducted according to the related guidelines and applicable laws in Japan.

2.2 | Antibody characterization

Please see TABLE 1 for a list of all antibodies used. These antibodies are listed in the “Journal of Comparative Neurology antibody database (Version 14)” except for the rabbit anti-glutamine synthetase (GS) antibody.

Glial fibrillary acidic protein (GFAP) Anti-GFAP rabbit serum (Chemicon, Temecula, CA) stains a single protein band of 51 kDa in the mouse brain on immunoblots (Jalil et al., 2005; Kawano, unpublished observations). This serum is also specific for GFAP on immunoblots in extracts from the mouse spinal cord (Darman et al., 2004) and rat retina (Chang et al., 2007). Astrocytes are immunolabeled with this antibody against GFAP (Morcos

and Chang-Ling, 2000).

The staining obtained with this anti-GFAP antibody in the rat was similar to published results on the rat (Saari et al., 1997; Morcos and Chang-Ling, 2000; Ju et al., 2005; Chang et al., 2007; Kawano, 2015).

Glutamine synthetase (GS) The rabbit anti-GS antibody (Sigma-Aldrich, Saint Louis, MO) recognizes a single protein band of 45 kDa in extracts from the rat brain. The staining of GS in immunoblotting is specifically inhibited with the GS immunizing peptide (amino acids 357-373 with N-terminally added lysine). This amino acid sequence is identical in human, bovine, rat, hamster, and pig GS, and is highly conserved in chicken GS (single amino acid substitution; manufacturer's technical information).

The mouse monoclonal anti-GS antibody (clone 6; BD Biosciences Pharmingen, San Diego, CA) visualizes a single protein band (45 kDa) in extracts from the rat brain on immunoblots (manufacturer's technical information). Müller cells in the retina and glial cells in the optic nerve are labeled with these antibodies against GS (Riepe and Norenburg, 1977).

The staining obtained with the two antibodies in the rat was similar to that previously reported in the mouse (Haverkamp and Wässle, 2000; Hojo et al., 2000; Kawano et al., 2008) and rat (Riepe and Norenburg, 1977; Zabouri et al., 2011; Kawano, 2015).

Myelin basic protein, human (MBPh) The mouse monoclonal antibody against the human myelin basic protein (clone SMI-99; Covance, Princeton, NJ) detects 4 bands between 14 and 21 kDa, corresponding to 4 myelin basic protein (MBP) isoforms on immunoblots of the rat cerebellum (Dyer et al., 1996; Talos et al., 2006). The SMI-99 antibody detects MBP from most mammalian species. The pig and chicken MBP do not react and the guinea pig MBP has slight reactivity. This antibody does not react with the 14kDa form of the rat MBP. The SMI-99 antibody detects the developing and adult myelin, and distinguishes oligodendrocytes from astrocytes, microglia, neurons and other cells in brain

sections (manufacturer's technical information).

The staining obtained with this antibody against the human myelin basic protein was similar to that previously reported in the rat (Morcos and Chang-Ling, 2000).

Neurofilament H non-phosphorylated The mouse monoclonal antibody against neurofilament H non-phosphorylated (clone SMI-32; Covance, Princeton, NJ) visualizes two bands (200 and 180 kDa) on conventional immunoblots, which merges into a single neurofilament H line on two-dimensional blots (Sternberger et al., 1982; Goldstein et al., 1983; Goldstein et al., 1987). The SMI-32 antibody reacts with a non-phosphorylated epitope from neurofilament H of most mammalian species. The reaction is masked when the epitope is phosphorylated (Sternberger and Sternberger, 1983). The SMI-32 antibody immunocytochemically visualizes neuronal cell bodies, dendrites, and some thick axons in the central and peripheral nervous systems, whereas thin axons are not revealed (manufacturer's technical information).

The staining obtained with this antibody against neurofilament H was similar to published results on the mouse (Howell et al., 2007) and rat (Kawano, 2015).

Oligodendrocytes Mature oligodendrocytes are immunostained with the mouse monoclonal antibody against oligodendrocytes [RIP] (clone NS-1; Chemicon; Friedman et al., 1989). The specificity of this antibody is strictly verified in the rat CNS (central nervous system; Friedman et al., 1989). Strong RIP staining is mainly confined to the white matter in the rat cerebellum, although moderate RIP staining is distributed in the granular layer. RIP staining is hardly detected in the molecular layer, which is composed of unmyelinated parallel fibers (Friedman et al., 1989).

The staining obtained with this antibody against oligodendrocytes [RIP] was similar to that previously reported in the rat (Saari et al, 1997; Morcos and Chang-Ling, 2000; Kawano, 2015).

2.3 | Immunohistochemistry

Sections were processed using double-label immunohistochemistry as previously described (Kawano et al., 2008; Kawano, 2015). Free-floating sections were pre-incubated for 2 hours with a 10% NGS blocking solution at 4 °C, and were then immunoreacted for 4 days with a mixture of rabbit and mouse primary antibodies in a 10% normal goat serum (NGS) blocking solution at 4 °C (TABLE 1). After two rinses for 10 minutes in 0.02M phosphate buffered saline (PBS) containing 0.3% Triton X-100 (PBST), the sections were incubated with a mixture of two secondary antibodies in PBS containing 5% NGS and 0.3% Triton X-100 for 24 hours at 4 °C. The two secondary antibodies used were Alexa Fluor 488 conjugated with the $F(ab')_2$ fragment of goat anti-rabbit IgG (H+L) (1:200; Molecular Probes, Eugene, OR) and Alexa Fluor 594 conjugated to the $F(ab')_2$ fragment of goat anti-mouse IgG (H+L) (1:200; Molecular Probes). The sections were washed once for 10 minutes in PBST, and then twice in PBS. The sections were mounted onto hydrophilic silanized slides (Dako Japan, Tokyo, Japan) in an equal-parts mixture of a 0.6% gelatin solution and PBS. After being air-dried, the sections were subjected to nuclear staining by using a bisBenzimide (bBM; Hoechst 33258, Sigma-Aldrich; 0.1 mg/ml) solution, and coverslipped with VECTASHIELD mounting medium (Vector Laboratories, Burlingame, CA).

In all cases, each staining protocol was performed on a minimum of 5 optic nerves from 5 separate rats. GFAP staining was done on a total of 11 optic nerves from 10 separate rats. GS staining was performed on 6 optic nerves from 6 separate rats. MBPh staining was done on 5 optic nerves from 5 separate rats. bBM staining was performed on a total of 14 optic nerves from 12 separate rats.

In order to eliminate the possibility of any cross-reaction between the secondary and primary antibodies from the wrong species, one of the two primary antibodies was removed.

No cross-reactivity was observed in these control experiments (data not shown).

2.4 | Photomicrographs

Fluorescent photomicrographs were taken with an LSM700 confocal laser scanning microscope (Carl Zeiss Jena GmbH, Jena, Germany) at the Joint Research Laboratory, Kagoshima University Graduate School of Medical and Dental Sciences. Images were transferred to Adobe Photoshop CS5 (Adobe Systems, San Jose, CA). The brightness and contrast of images were adjusted. No other adjustment was made.

2.5 | Image Analysis

The quantitation of all images was performed using ImageJ2 (Version 2.9.0/1.53t; developed by Wayne Rasband, National Institute of Mental Health, Bethesda, MD, USA).

2.6 | Measurement of area of each region, and that of mean pixel intensity of GFAP immunoreactivity in each region

Confocal microscopic images of GFAP immunoreactivity were assembled using a photomerge function in Adobe Photoshop CS5 (Layout; Reposition; FIGURE 1A, B). Measurements were performed in the shaded area of each region depicted in FIGURE 1C and 1D. The area is also shown in GFAP immunoreactivity image of each region in FIGURE 3. Before measurements, the color channels were split in order to obtain the green channel, we cut the background off the measurement area (FIGURE 3). For each image, the process performed by the ImageJ2 program included the following: (a) setting the threshold 1-255 in order to binarize the image (Manual); (b) analyzing particles to measure area and mean pixel intensity (size, 100 μm^2-infinity; circularity, 0.00-1.00; check “Clear results”, and “Add to manager”).

2.7 | Measurement of area and mean pixel intensity of GFAP-immunoreactive filaments in each region

For each image, the process performed by the ImageJ2 program included the following: (a) establishing the threshold in order to binarize the image (Auto (Default) or Manual); (b) analyzing particles to measure area, and mean pixel intensity of GFAP immunoreactive filaments (size, 0 μm^2-infinity; circularity, 0.00-1.00; check "Clear Results", and "Add to manager").

Mean pixel intensity of GFAP-immunoreactive filaments in each region was weighted average, which was manually calculated based on the outputs of the measurement processes described above (mean pixel intensity of each GFAP-immunoreactive filament and an area of each GFAP-immunoreactive filament).

2.8 | Measurement of proportion of total area of GFAP-immunoreactive filaments in each region

Proportion of total area of GFAP-immunoreactive filaments was manually calculated based on the total of area of each GFAP-immunoreactive filament, and on the area of each region.

2.9 | Measurement of area of each region, and that of mean pixel intensities of GS immunoreactivity, bBM labeling, and of MBPh immunoreactivity in each region

Confocal microscopic images of GS immunoreactivity, bBM labeling, and of MBPh immunoreactivity were assembled manually in Adobe Photoshop CS5 (FIGURE 2). Measurements were performed in the shaded area of each region depicted in FIGURE 1C and 1D. The areas that the measurements were performed are also shown in GS immunoreactivity

images of each region in FIGURE 4, in bBM labeling images of each region in FIGURE 5, and in MBPh immunoreactivity images of each region in FIGURE 6. Before the measurements, the color channels were split in order to obtain the green channel for GS immunoreactivity image, the blue channel for bBM labeling image, and the red channel for MBPh immunoreactivity image, we cut the background off the measurement area (FIGURES 4-6). For each image, the process performed by the ImageJ2 program included the following: (a) setting the threshold 1-255 in order to binarize the image (Manual); (b) analyzing particles to measure area and mean pixel intensity (size, 1.0 μm^2-infinity; circularity, 0.00-1.00; check "Clear results", and "Add to manager").

2.10 | Counts of GS-immunoreactive cells, bBM-labeled cell nuclei, and of MBPh-immunoreactive particles

GS-immunoreactive cells, bBM-labeled cell nuclei, and MBPh-immunoreactive particles were counted in the shaded area of each region depicted in FIGURE 1C and 1D.

GS-immunoreactive cells The brightness and contrast of images were adjusted for cell count. We open a Photoshop image file in Adobe Illustrator CS5 (Adobe Systems, San Jose, CA) by using the Place function. We draw a small closed circle, above each soma of GS immunoreactive cell, on upper layer in Illustrator CS5. We count small closed circles to obtain number of GS-immunoreactive cells by selecting the circles; number of the circles were displayed in the Objects item of the Document Info panel in Illustrator CS5. The morphological characteristics of GS-immunoreactive cells were as follows: 1) GS immunoreactivity was clearly seen in the cell body of the GS-immunoreactive cell; 2) The area of the cell nucleus was encircled by strong-to-moderate GS immunoreactivity; 3) Weak GS immunoreactivity was seen in the area of cell nucleus; 4) All part of the cell body was located in the measurement area.

bBM labeled cell nuclei For each image, the process performed by the ImageJ2 program included the following: (a) performing the Subtract Background function to remove smooth continuous backgrounds from the image (Rolling Ball Algorithm; Radius: 50.0 pixels); (b) doing the Median filter function to reduce noise in the image (Radius: 2.0 pixels); (c) performing the Mean filter function to smooth the image (Radius: 2.0 pixels); (d) establishing the threshold in order to binarize the image (Auto; Default); (e) applying the watershed; (f) analyzing particles to count cell nuclei (size: 7.0 μm^2-infinity; circularity: 0.00-1.00; check "Clear Results", "Add to manager", "Exclude on edges", and "Include holes").

MBPh-immunoreactive particles For each image, the process performed by the ImageJ2 program included the following: (a) establishing the threshold in order to binarize the image (Manual); (b) analyzing particles to count MBPh-immunoreactive particles (size: 1.0 μm^2-infinity; circularity 0.00-1.00; check "Clear results", "Add to manager", and "Exclude on edges").

2.11 | Measurement of density of GS-immunoreactive cells, bBM-labeled cell nuclei, and of MBPh-immunoreactive particles

Density of GS-immunoreactive cells, bBM labeled cell nuclei, and of MBPh-immunoreactive particles was manually calculated based on the outputs of the count processes and on the area of each region.

2.12 | Measurement of mean area and mean pixel intensity of GS-immunoreactive cells

For each image, the process performed by the ImageJ2 program included the following: (a) performing the Subtract Background function to remove smooth continuous

background from the image (Rolling Ball Algorithm; Radius: 50.0 pixels); (b) Performing the Median filter function to reduce noise in the image (Radius: 2.0 pixels); (c) Performing the Mean filter function to smooth the image (Radius: 2.0 pixels); (d) establishing the threshold in order to binarize the image (Auto (Default) or Manual); (e) analyzing particles to measure area and mean pixel intensity of GS-immunoreactive cells (size: 1.0 μm^2-infinity; circularity: 0.00-1.00; check "Clear Results", "Add to manager", "Exclude on edges" and "Include holes").

Mean area of GS-immunoreactive cells in each region was manually calculated based on the outputs of the measurement processes described above (total area of GS-immunoreactive cells in each region) and on the count processes (total number of GS-immunoreactive cells in each region).

Mean pixel intensity of GS-immunoreactive cells in each region was weighted average, which was manually calculated based on the outputs of the measurement processes described above (area and mean pixel intensity of each GS-immunoreactive cell).

2.13 | Measurement of mean area and mean pixel intensity of bBM-labeled cell nuclei

For each image, the process performed by the ImageJ2 program included the following: (a) performing the Subtract Background function to remove smooth continuous background from the image (Rolling Ball Algorithm; Radius: 50.0 pixels); (b) Performing the Median filter function to reduce noise in the image (Radius: 2.0 pixels); (c) Performing the Mean filter function to smooth the image (Radius: 2.0 pixels); (d) establishing the threshold in order to binarize the image (Auto; Default); (e) applying the watershed; (f) analyzing particles to measure area and mean pixel intensity of each bBM-labeled cell nucleus, and to

count bBM-labeled cell nuclei (size: 7.0 μm^2-infinity; circularity: 0.00-1.00; check “Clear Results”, “Add to manager”, “Exclude on edges” and “Include holes”).

Mean area of bBM-labeled cell nuclei in each region was manually calculated based on the outputs of the measurement processes described above (area of each bBM-labeled cell nucleus and number of bBM-labeled cell nuclei).

Mean pixel intensity of bBM-labeled cell nuclei in each region was weighted average, which was manually calculated based on the outputs of the measurement processes described above (area and mean pixel intensity of each bBM-labeled cell nucleus).

2.14 | Measurement of mean pixel intensity, mean area, mean perimeter, and mean shape descriptors of MBPh-immunoreactive particles

For each image, the process performed by the ImageJ2 program included the following: (a) establishing the threshold in order to binarize the image (Manual); (b) analyzing particles to obtain mean pixel intensity, area, perimeter, and shape descriptors (Circularity; AR (aspect ratio); Roundness; Solidity) of each MBPh-immunoreactive particle, and to count MBPh-immunoreactive particles (size: 1.0 μm^2-infinity; circularity 0.00-1.00; check “Clear results”, “Add to manager”, and “Exclude on edges”).

Mean pixel intensity of MBPh-immunoreactive particles in each region was weighted average, which was manually calculated based on the outputs of the measurement processes described above (area and mean pixel intensity of each MBPh-immunoreactive particle).

Mean area, mean perimeter, and mean shape descriptors of MBPh-immunoreactive particles were manually calculated based on the outputs of the measurement processes described above (area, perimeter, Circularity, AR, Roundness, and Solidity of each MBPh-immunoreactive particle, and number of MBPh-immunoreactive particles).

2.15 | Measurement of proportion of total areas of GS-immunoreactive cells, bBM-labeled cell nuclei, and of MBPh-immunoreactive particles

Proportion of total areas of GS-immunoreactive cells, bBM labeled cell nuclei, and of MBPh-immunoreactive particles were manually calculated based on the output of measurement processes of area of each GS-immunoreactive cell, bBM-labeled cell nucleus, and of each MBPh-immunoreactive particle and on the area of each region.

2.16 | Statistical Analysis

No statistical methods were used to predetermine group sample size. However, our group sample sizes were similar to previously published studies by our group and others (Melo et al., 2006; Balaratnasingam et al., 2009; Kawano, 2015). All biological replicates (n) are derived at least five independent experiments. Unless otherwise specified, no data were excluded from analysis. Individual experiment values are shown on box-and-whisker plots. In box-and-whisker plots, center lines indicate medians, box edges represent the interquartile range, and whisker extend down to the minimum and up to the maximum of the distribution.

All statistical analyses were performed with EZR (Easy R; Version 1.55; Saitama Medical Center, Jichi Medical University, Saitama, Japan), which is a graphical user interface for R (Version 4.1.3; The R Foundation for Statistical Computing, Vienna, Austria). More precisely, it is a modified version of R commander (Version 2.7-2; Fox, 2017) designed to add statistical functions frequently used in biostatistics (Kanda, 2013). Data were analyzed by the Kruskal-Wallis test with the Steel-Dwass test for multiple comparisons. $P < 0.05$ was considered significant.

3 | RESULTS

3.1 | Division of the normal rat optic nerve

A definition of the optic nerve division was necessary for the description and interpretation of experimental results; therefore, we described our criteria for determining the border of each region of the optic nerve. The criteria principally followed our previously reported rat criteria except for subregions in the myelinated region (Kawano, 2015).

As shown in FIGURE 1A, the rat optic nerve in the orbit was divided into three regions: the intraretinal (i), unmyelinated (u), and myelinated (m) regions. This classification was defined by the position of the sensory retina, the distribution of oligodendrocytes (myelinated nerve fibers), and by the strength of GFAP immunoreactivity. The border between the i and u regions was set at the boundary between the sensory retina and retinal pigment epithelium. Very strong GFAP immunoreactivity was observed in the u region. The border between the u and m regions was defined by the distal limit of myelinated nerve fibers (FIGURE 1A). This border principally coincided with the boundary defined by the proximal limit of very strong GFAP immunoreactivity; however, protrusions of myelinated nerve fibers were observed in the posterior part of the u region (FIGURE 1A, B). The border between the nerve fiber layer of the retina (NFL) and the optic nerve proper was set at the medial margin of the distribution area of strong GS immunoreactivity in the NFL (Kawano, 2015; FIGURE 2A, B).

3.2 | Division and general overview of the myelinated (m) region in the normal rat optic nerve

The m region was further divided into two subregions: myelinated regions 1 (m1) and 2 (m2; FIGURE 1). The longitudinal length of each subregion was set at 1mm. Accordingly,

the boundary between the m1 and m2 regions was set at the line to which a distance from the border between the unmyelinated and myelinated regions (distance from the u/m border) was 1mm. The proximal boundary of the m2 region was set at the line to which a distance from the u/m border was 2 mm. The m1 region was divided into 4 sub-subregions: myelinated regions 1a (m1a), 1b (m1b), 1c (m1c), and 1d (m1d). The longitudinal length of each sub-subregion was 250 μm (FIGURE 1D). The m1 region was also divided into 2 sub-subregions: myelinated regions 1ab (m1ab), and 1cd (m1cd). The longitudinal length of each sub-subregion was 500 μm (FIGURE 1C). The m2 region was divided into 2 sub-subregions: myelinated regions 2ab (m2ab), and 2cd (m2cd). The longitudinal length of each sub-subregion was 500 μm (FIGURE 1C).

The m1ab region was thicker than the other three myelinated regions: the m1cd, m2ab, and m2cd regions (FIGURES 1-2).

Densely packed myelinated (RIP-immunoreactive) nerve fiber bundles (FIGURE 1A) and GFAP-poor tracks (FIGURE 1B) were observed in the m2cd region. In the GFAP-poor tracks, densely packed myelinated nerve fiber bundles were located (FIGURE 1A, B). Weak GS-immunoreactivity was seen in the m2cd region (FIGURE 2B). Moderately packed myelinated nerve fiber bundles were observed in the m1ab region (FIGURE 1A). Columns of GFAP-immunoreactive cells were observed to be interdigitate with the myelinated nerve fiber bundles (FIGURE 1A, B). GFAP-rich tracks (FIGURE 1B) were observed in the m1ab region. In the GFAP-rich tracks, moderately packed myelinated nerve fiber bundles were located (FIGURE 1A, B). Moderate GS-immunoreactivity was clearly seen in the m1ab region (FIGURE 2B). Chemoarchitecture of GFAP, GS, and RIP in the m2ab region was similar to that in the m2cd region. As for chemoarchitecture of GFAP, GS, and of RIP, the m1cd region was seen to be the transitional area between the m1ab and m2ab regions (FIGURES 1-2).

3.3 | GFAP and GFAP-immunoreactive filaments

The m1ab region was the major site of GFAP immunoreactivity localization and the major distribution area of GFAP-immunoreactive filaments in the myelinated region of the normal rat optic nerve (FIGURE 1, 3, 7).

The intensity of GFAP immunoreactivity was strong in the m1ab region, moderate in the m1cd region, and weak in both the m2ab and m2cd regions. Statistical analyses revealed significant differences in the intensity between the m1ab and m1cd regions, and between the m1cd and m2ab regions (the Kruskal-Wallis test with the Steel-Dwass test for multiple comparison, $P=0.027<0.05$ or $P=0.045<0.05$, $n=5$). However, there was no significant difference in the intensity between the m2ab and m2cd regions (FIGURE 7A). In the m1 region, the intensity of GFAP immunoreactivity was the strongest in the m1a region with a gradual decrease in the intensity along the proximal course of the optic nerve. Statistical analyses revealed significant differences in the intensity between the m1a and m1b regions, and between the m1c and m1d regions (the Kruskal-Wallis test with the Steel-Dwass test for multiple comparison, $P=0.027<0.05$ or $P=0.045<0.05$, $n=5$). However, there was no significant difference in the intensity between the m1b and m1c regions (FIGURE 7D).

The proportion of total area of GFAP-immunoreactive filaments was high in the m1ab region, moderate in the m1cd region, and low in both the m2ab and m2cd regions. Statistical analyses revealed significant differences in the proportion between the m1ab and m1cd regions, and between the m1cd and m2ab regions (the Kruskal-Wallis test with the Steel-Dwass test for multiple comparison, $P=0.027<0.05$ or $P=0.045<0.05$, $n=5$). However, there was no significant difference in the proportion between the m2ab and m2cd regions (FIGURE 7C). In the m1 region, the proportion of total area of GFAP-immunoreactive filaments was higher in both the m1a and m1b regions, but lower in both the m1c and m1d

regions. Statistical analyses revealed significant differences in the proportion between the m1b and m1c regions (the Kruskal-Wallis test with the Steel-Dwass test for multiple comparison, P=0.027<0.05 or P=0.045<0.05, n=5). However, there was no significant difference in the proportion between the m1a and m1b regions, and between m1c and m1d regions (FIGURE 7F).

The intensity of GFAP immunoreactivity in GFAP-immunoreactive filaments was largely constant from the m1ab region through the m2cd region. Statistical analyses revealed no significant difference in the intensity among the m1ab, m1cd, m2ab, and m2cd regions (the Kruskal-Wallis test with the Steel-Dwass test for multiple comparison, P≧0.05, n=5; FIGURE 7B). In the m1 region, the intensity of GFAP immunoreactivity in GFAP-immunoreactive filaments was also largely constant from the m1a region through the m1d region. Statistical analyses revealed no significant difference in the intensity among the m1a, m1b, m1c, and m1d regions (the Kruskal-Wallis test with the Steel-Dwass test for multiple comparison, P≧0.05, n=5; FIGURE 7E).

3.4 | GS and GS-immunoreactive cells

The m1ab region was the major site of GS immunoreactivity localization in the myelinated region of the normal rat optic nerve (FIGURES 2, 4, 8).

The intensity of GS immunoreactivity was strong in the m1ab region, moderate in the m1cd region, and weak in both the m2ab and m2cd regions. Statistical analyses revealed significant differences in the intensity between the m1ab and m1cd regions, and between the m1cd and m2ab regions (the Kruskal-Wallis test with the Steel-Dwass test for multiple comparison, P=0.027<0.05 or P=0.045<0.05, n=5). However, there was no significant difference in the intensity between the m2ab and m2cd regions (FIGURE 8A). In the m1 region, the intensity of GS immunoreactivity was the strongest in the m1a region, moderate

in the m1b region, and the weakest in both the m1c and m1d regions. Statistical analyses revealed significant differences in the intensity between the m1a and m1b regions, and between the m1b and m1c regions (the Kruskal-Wallis test with the Steel-Dwass test for multiple comparison, P=0.027<0.05 or P=0.045<0.05, n=5). However, there was no significant difference in the intensity between the m1c and m1d regions (FIGURE 8F).

The intensity of GS immunoreactivity in GS-immunoreactive cells was strong in the m1ab region, and moderate in the other 3 regions: the m1cd, m2ab, and m2cd regions. Statistical analyses revealed significant differences in the intensity between the m1ab and m1cd regions, between the m1ab and m2ab regions, and between the m1ab and m2cd regions (the Kruskal-Wallis test with the Steel-Dwass test for multiple comparison, P=0.027<0.05, n=5). However, there was no significant difference in the intensity among the m1cd, m2ab, and m2cd regions (FIGURE 8B). In the m1 region, the intensity of GS immunoreactivity in GS-immunoreactive cells was strong in the m1a region, strong-to-moderate in the m1b region, and moderate in both the m1c and m1d regions. Statistical analyses revealed significant differences in the intensity between the m1a and m1c regions, and between the m1a and m1d regions (the Kruskal-Wallis test with the Steel-Dwass test for multiple comparison, P=0.027<0.05, n=5). However, there was no significant difference in the intensity between the m1a and m1b regions, between the m1b and m1c regions, and between the m1c and m1d regions (FIGURE 8G).

The proportion of total area of GS-immunoreactive cells was large in the m1ab region, large-to-medium in the m1cd region, and medium in the m2ab and m2cd regions. Statistical analyses revealed significant difference in the proportion between the m1ab and m2ab regions, and between the m1ab and m2cd regions (the Kruskal-Wallis test with the Steel-Dwass test for multiple comparison, P=0.027<0.05, n=5). However, there was no significant difference in the intensity between the m1ab and m1cd regions, between the m1cd

and m2ab regions, and between the m2ab and m2cd regions (FIGURE 8C). In the m1 region, the proportion of total area of GS-immunoreactive cells was largely constant from the m1a region through the m1d region. Statistical analyses revealed no significant difference in the proportion among the m1a, m1b, m1c, and m1d regions (the Kruskal-Wallis test with the Steel-Dwass test for multiple comparison, P≧0.05, n=5; FIGURE 8H).

The mean area of GS-immunoreactive cells was large in the m1ab region, large-to-medium in the m1cd and m2ab regions, and medium in the m2cd region. Statistical analyses revealed significant differences in the mean area between the m1ab and m2cd regions (the Kruskal-Wallis test with the Steel-Dwass test for multiple comparison, P=0.027<0.05, n=5). However, there was no significant difference in the mean area between the m1ab and m1cd regions, between the m1cd and m2ab regions, and between the m2ab and m2cd regions (FIGURE 8E). In the m1ab region, the mean area of GS-immunoreactive cells in the m1a region was larger than that in the m1b region. Statistical analyses revealed significant differences in the mean area between the m1a and m1b regions (the Kruskal-Wallis test with the Steel-Dwass test for multiple comparison, P=0.027<0.05, n=5; FIGURE 8J).

The density of GS-immunoreactive cells was largely constant from the m1ab region through the m2cd region. Statistical analyses revealed no significant difference in the density among the m1ab, m1cd, m2ab, and m2cd regions (the Kruskal-Wallis test with the Steel-Dwass test for multiple comparison, P≧0.05, n=5; FIGURE 8D). In the m1 region, the density of GS-immunoreactive cells was also largely constant from the m1a region through the m1d region. Statistical analyses revealed no significant difference in the density among the m1a, m1b, m1c, and m1d regions (the Kruskal-Wallis test with the Steel-Dwass test for multiple comparison, P≧0.05, n=5; FIGURE 8I).

Interestingly, the m1a region was the major site of GS distribution in the myelinated region of the normal rat optic nerve; however, GS immunoreactivity in this region was markedly weaker than that in the retina (FIGURES 2A, G, 8A, F).

3.5 | bBM and bBM-labeled cell nuclei

The m1ab region was the major site of bBM labeling localization in the myelinated region of the normal rat optic nerve (FIGURES 2, 5, 9).

The intensity of bBM labeling was strong in the m1ab region, and moderate in the other 3 regions: the m1cd, m2ab, and m2cd regions. Statistical analyses revealed significant differences in the intensity between the m1ab and m1cd regions, between the m1ab and m2ab regions, and between the m1ab and m2cd regions (the Kruskal-Wallis test with the Steel-Dwass test for multiple comparison, $P=0.027<0.05$, $n=5$). However, there was no significant difference in the intensity among the m1cd, m2ab, and m2cd regions (FIGURE 9A). In the m1 region, the intensity of bBM labeling was strong in the m1a region, strong-to-moderate in the m1b region, and moderate in the m1c and m1d regions. Statistical analyses revealed significant differences in the intensity between the m1a and m1c regions, and between the m1a and m1d regions (the Kruskal-Wallis test with the Steel-Dwass test for multiple comparison, $P=0.027<0.05$, $n=5$). However, there was no significant difference in the intensity between the m1a and m1b regions, between the m1b and m1c regions, and between the m1c and m1d regions (FIGURE 9F).

The intensity of bBM labeling in bBM-labeled cell nuclei was strong in the m1ab region, strong-to-moderate in the m1cd and m2ab regions, and moderate in the m2cd region. Statistical analyses revealed significant difference in the intensity between the m1ab and m2cd regions (the Kruskal-Wallis test with the Steel-Dwass test for multiple comparison, $P=0.027<0.05$, $n=5$). However, there was no significant difference in the intensity among the

m1ab, m1cd, and m2ab regions (FIGURE 9B). In the m1 region, the intensity of bBM labeling in bBM-labeled cell nuclei was largely constant from the m1a region through the m1d region. Statistical analyses revealed no significant difference in the intensity among the m1a, m1b, m1c, and m1d regions (the Kruskal-Wallis test with the Steel-Dwass test for multiple comparison, P≧0.05, n=5; FIGURE 9G).

The proportion of total area of bBM labeled cell nuclei was large in the m1ab region, and medium in the other 3 regions: the m1cd, m2ab, and m2cd regions. Statistical analyses revealed significant differences in the proportion between the m1ab and m1cd regions, between the m1ab and m2ab regions, and between the m1ab and m2cd regions (the Kruskal-Wallis test with the Steel-Dwass test for multiple comparison, P=0.027<0.05, n=5). However, there was no significant difference in the proportion among the m1cd, m2ab, and m2cd regions (FIGURE 9C). In the m1 region, the proportion of total area of bBM-labeled cell nuclei was large in the m1a region, large-to-medium in the m1b region, and medium in the m1c and m1d regions. Statistical analyses revealed significant differences in the proportion between the m1a and m1c regions, and between the m1a and m1d regions (the Kruskal-Wallis test with the Steel-Dwass test for multiple comparison, P=0.027<0.05, n=5). However, there was no significant difference in the proportion between the m1a and m1b regions, between the m1b and m1c regions, and between the m1c and m1d regions (FIGURE 9H).

The density of bBM-labeled cell nuclei was high in the m1ab region, and medium in the other 3 regions: the m1cd, m2ab, and m2cd regions. Statistical analyses revealed significant differences in the density of bBM-labeled cell nuclei between the m1ab and m1cd regions, between the m1ab and m2ab regions, and between the m1ab and m2cd regions (the Kruskal-Wallis test with the Steel-Dwass test for multiple comparison, P=0.027<0.05, n=5). However, there was no significant difference in the density among the m1cd, m2ab, and m2cd regions (FIGURE 9D). In the m1 region, the density of bBM-labeled cell nuclei was

high in the m1a region, high-to-medium in the m1b region, and medium in the m1c and m1d regions. Statistical analyses revealed significant differences in the density between the m1a and m1c regions, and between the m1a and m1d regions (the Kruskal-Wallis test with the Steel-Dwass test for multiple comparison, P=0.027<0.05, n=5). However, there was no significant difference in the density between the m1a and m1b regions, between the m1b and m1c regions, and between the m1c and m1d regions (FIGURE 9I).

The mean area of bBM-labeled cell nuclei was largely constant from the m1ab region through the m2cd region. Statistical analyses revealed no significant difference in the mean area among the m1ab, m1cd, m2ab, and m2cd regions (the Kruskal-Wallis test with the Steel-Dwass test for multiple comparison, P≧0.05, n=5; FIGURE 9E). In the m1ab region, the mean area of bBM-labeled cell nuclei in the m1a region was larger than that in the m1b region. Statistical analyses revealed significant difference in the mean area between the m1a and m1b regions (the Kruskal-Wallis test with the Steel-Dwass test for multiple comparison, P=0.027<0.05, n=5; FIGURE 8J).

3.6 | MBPh and MBPh-immunoreactive particles

The m1ab region, especially the m1a region, were the major sites of MBPh-immunoreactive-particle-localization in the myelinated region of the normal rat optic nerve (FIGURES 2, 6, 10).

The intensity of MBPh immunoreactivity was largely constant from the m1ab region through the m2cd region. Statistical analyses revealed no significant difference in the intensity among the m1ab, m1cd, m2ab, and m2cd regions (the Kruskal-Wallis test with the Steel-Dwass test for multiple comparison, P≧0.05, n=5; FIGURE 10A). In the m1 region, the intensity of MBPh immunoreactivity was largely constant from the m1a region through the m1d region. Statistical analyses revealed no significant difference in the intensity among the

m1a, m1b, m1c, and m1d regions (the Kruskal-Wallis test with the Steel-Dwass test for multiple comparison, P≧0.05, n=5; FIGURE 10G).

The intensity of MBPh immunoreactivity in MBPh-immunoreactive particles was strong in the m1ab region, strong-to-moderate in the m1cd region, and moderate in the m2ab and m2cd regions. Statistical analyses revealed significant differences in the intensity between the m1ab and m2ab regions, and between the m1ab and m2cd regions (the Kruskal-Wallis test with the Steel-Dwass test for multiple comparison, P=0.027<0.05, n=5). However, there was no significant difference in the intensity between the m1ab and m1cd regions, between the m1cd and m2ab regions, and between the m2ab and m2cd regions (FIGURE 10B). In the m1 region, the intensity of MBPh immunoreactivity in MBPh-immunoreactive particles was strong in the m1a region, strong-to-moderate in the m1c region, and moderate in the m1b and m1d regions. Statistical analyses revealed significant differences in the intensity between the m1a and m1b regions, and between the m1a and m1d regions (the Kruskal-Wallis test with the Steel-Dwass test for multiple comparison, P=0.027<0.05, n=5). However, there was no significant difference in the intensity between the m1a and m1c regions, between the m1b and m1c regions, and between the m1c and m1d regions (FIGURE 10H).

The proportion of total area of MBPh-immunoreactive particles was large in the m1ab region, but small in the other 3 regions: the m1cd, m2ab, and m2cd regions. Statistical analyses revealed significant differences in the proportion between the m1ab and m1cd regions, between the m1ab and m2ab regions, and between the m1ab and m2cd regions (the Kruskal-Wallis test with the Steel-Dwass test for multiple comparison, P=0.027<0.05, n=5). However, there was no significant difference in the proportion among the m1cd, m2ab, and m2cd regions (FIGURE 10C). In the m1 region, the proportion of total area of MBPh-immunoreactive particles was large in the m1a region, medium-to-small in the m1b region,

and small in the m1c and m1d regions. Statistical analyses revealed significant differences in the proportion between the m1a and m1b regions, between the m1a and m1c regions, and between the m1a and m1d regions (the Kruskal-Wallis test with the Steel-Dwass test for multiple comparison, P=0.027<0.05, n=5). However, there was no significant difference in the proportion among the m1b, m1c, and m1d regions (FIGURE 10I).

The density of MBPh-immunoreactive particles was high in the m1ab region, but low in the other 3 regions: the m1cd, m2ab, and m2cd regions. Statistical analyses revealed significant differences in the density of MBPh-immunoreactive particles between the m1ab and m1cd regions, between the m1ab and m2ab regions, and between the m1ab and m2cd regions (the Kruskal-Wallis test with the Steel-Dwass test for multiple comparison, P=0.027<0.05, n=5). However, there was no significant difference in the density among the m1cd, m2ab, and m2cd regions (FIGURE 10D). In the m1 region, the density of MBPh-immunoreactive particles was high in the m1a region, medium-to-low in the m1b region, and low in the m1c and m1d regions. Statistical analyses revealed significant differences in the density between the m1a and m1b regions, between the m1a and m1c regions, and between the m1a and m1d regions (the Kruskal-Wallis test with the Steel-Dwass test for multiple comparison, P=0.027<0.05, n=5). However, there was no significant difference in the density among the m1b, m1c, and m1d regions (FIGURE 10J).

The mean area of MBPh-immunoreactive particles was large in the m1ab region, medium in the m1cd and m2ab regions, and large-to-medium in the m2cd region. Statistical analyses revealed significant differences in the mean area between the m1ab and m1cd regions, and between the m1ab and m2ab regions (the Kruskal-Wallis test with the Steel-Dwass test for multiple comparison, P=0.027<0.05, n=5). However, there was no significant difference in the mean area between the m1ab and m2cd regions. In addition, there was no significant difference in the mean area among the m1cd, m2ab, and m2cd regions (FIGURE

10E). In the m1 region, the mean area of MBPh-immunoreactive particles was large in the m1a region, and medium in the other three regions: m1b, m1c, and m1d regions. Statistical analyses revealed significant differences in the mean area between the m1a and m1b regions, between the m1a and m1c regions, and between the m1a and m1d regions (the Kruskal-Wallis test with the Steel-Dwass test for multiple comparison, P=0.027<0.05, n=5). However, there was no significant difference in the mean area among the m1b, m1c, and m1d regions (FIGURE 10K).

The mean perimeter of MBPh-immunoreactive particles was long in the m1ab region, medium in the m1cd and m2ab regions, and long-to-medium in the m2cd region. Statistical analyses revealed significant differences in the mean perimeter between the m1ab and m1cd regions, and between the m1ab and m2ab regions (the Kruskal-Wallis test with the Steel-Dwass test for multiple comparison, P=0.027<0.05, n=5). However, there was no significant difference in the mean perimeter between the m1ab and m2cd regions. In addition, there was no significant difference in the mean perimeter among the m1cd, m2ab, and m2cd regions (FIGURE 10F). In the m1 region, the mean perimeter of MBPh-immunoreactive particles was long in the m1a region, and medium in the other three regions: the m1b, m1c, and m1d regions. Statistical analyses revealed significant differences in the mean perimeter between the m1a and m1b regions, between the m1a and m1c regions, and between the m1a and m1d regions (the Kruskal-Wallis test with the Steel-Dwass test for multiple comparison, P=0.027<0.05, n=5). However, there was no significant difference in the mean perimeter among the m1b, m1c, and m1d regions (FIGURE 10L).

Interestingly, MBPh-immunoreactive particles were densely distributed in the m1ab region, especially in the m1a region, however, these were sparsely dispersed in the m1cd, m2ab, and in the m2cd regions (FIGURE 10).

3.7 | Shape descriptors of MBPh-immunoreactive particles

Shape descriptors, such as circularity, AR (aspect ratio), roundness, and solidity, of MBPh-immunoreactive particles were primarily stable from the m1ab region through the m2cd region and from the m1a region through the m1d region except for the circularity in the m1 region (FIGURE 11).

The mean circularity was medium in the m1ab region, large in the m1cd region, and small-to-large in the m2ab and m2cd regions. Statistical analyses revealed significant difference in the mean circularity between the m1ab and m1cd regions (the Kruskal-Wallis test with the Steel-Dwass test for multiple comparison, $P=0.027<0.05$, $n=5$). However, there was no significant difference in the mean circularity among the m1cd, m2ab, and m2cd regions (FIGURE 11A). In the m1 region, the mean circularity was medium in the m1a region, medium-to-large in the m1b and m1c regions, and large in the m1d region. Statistical analyses revealed significant difference in the mean circularity between the m1a and m1d regions (the Kruskal-Wallis test with the Steel-Dwass test for multiple comparison, $P=0.027<0.05$, $n=5$). However, there was no significant difference in the mean circularity between the m1a and m1b regions, between the m1b and m1c regions, and between the m1c and m1d regions (FIGURE 11E).

The mean AR of MBPh-immunoreactive particles was largely constant from the m1ab region through the m2cd region. Statistical analyses revealed no significant difference in the mean AR among the m1ab, m1cd, m2ab, and m2cd regions (the Kruskal-Wallis test with the Steel-Dwass test for multiple comparison, $P\geqq0.05$, $n=5$; FIGURE 11B). In the m1 region, the mean AR of MBPh-immunoreactive particles was also largely constant from the m1a region through the m1d region. Statistical analyses revealed no significant difference in the mean AR among the m1a, m1b, m1c, and m1d regions (the Kruskal-Wallis test with the Steel-Dwass test for multiple comparison, $P\geqq0.05$, $n=5$; FIGURE 11F).

The mean roundness was medium in the m1ab region, large in the m1cd region, and small-to-large in the m2ab and m2cd regions. Statistical analyses revealed significant difference in the mean roundness between the m1ab and m1cd regions (the Kruskal-Wallis test with the Steel-Dwass test for multiple comparison, $P=0.027<0.05$, $n=5$). However, there was no significant difference in the mean circularity among the m1cd, m2ab, and m2cd regions (FIGURE 11C). In the m1 region, the mean roundness was largely constant from the m1a region through the m1d region. Statistical analyses revealed no significant difference in the mean roundness among the m1a, m1b, m1c, and m1d regions (the Kruskal-Wallis test with the Steel-Dwass test for multiple comparison, $P \geqq 0.05$, $n=5$; FIGURE 11G).

The mean solidity of MBPh-immunoreactive particles was largely constant from the m1ab region through the m2cd region. Statistical analyses revealed no significant difference in the mean solidity among the m1ab, m1cd, m2ab, and m2cd regions (the Kruskal-Wallis test with the Steel-Dwass test for multiple comparison, $P \geqq 0.05$, $n=5$; FIGURE 11D). In the m1 region, the mean solidity of MBPh-immunoreactive particles was medium in the m1a region, medium-to-large in the m1c region, and large in the m1b and m1d regions. Statistical analyses revealed significant difference in the mean solidity between the m1a and m1b regions, and between the m1a and m1d regions (the Kruskal-Wallis test with the Steel-Dwass test for multiple comparison, $P=0.027<0.05$, $n=5$). However, there was no significant difference in the mean solidity between the m1a and m1c regions. In addition, there was no significant difference in the mean solidity among the m1b, m1c, and m1d regions (FIGURE 11H).

4 | DISCUSSION

4.1 | Summary of results

We determined the distribution pattern of the glial cell proteins (GFAP, MBPh, and GS) and the cell nucleus marker (bBM) in the myelinated region of the normal rat optic nerve. In addition, we analyzed the distribution pattern and the shape descriptors of MBPh-immunoreactive particles in this region. GFAP immunoreactivity and GS immunoreactivity were significantly strong in the m1ab region, moderate in the m1cd region, and weak in the m2ab and m2cd regions. Similar to the distribution patterns of GFAP immunoreactivity and of GS immunoreactivity, bBM labeling was significantly strong in the m1ab region, and moderate in the m1cd region, however, bBM labeling was also moderate in the m2ab and m2cd regions. Different from these findings, MBPh immunoreactivity was largely constant from the m1ab region through the m2cd region. Interestingly, MBPh-immunoreactive particles were densely distributed in the m1ab region, especially in the m1a region, however, these particles were loosely dispersed in the m1cd, m2ab, and m2cd regions. The shape descriptors of the particles were primarily stable from the m1ab region through the m2cd region except for the circularity in the m1 region.

4.2 | Comparison with previous findings

The division scheme used in this study was principally compatible with a previous study in the rat except for the subregions in the myelinated region (Kawano, 2015). In both studies, the myelinated region was divided into two subregions: the m1 and m2 regions. In the previous study, the border between the m1*[2] and m2* regions was defined by the shape

[2] To distinguish the m1 and m2 regions in the present study from those in the previous study (Kawano, 2015), each subregion in the previous study is labeled with "*": m1* and m2*.

of the outline in the myelinated region. The longitudinal length of the m1* region was 872.2 ± 30.9 μm (Average ± SE; n = 5; Kawano, 2015). In the present study, the boundary between the m1 and m2 regions was set at the line to which a distance from the u/m border (border between the unmyelinated and myelinated regions) was 1 mm. In addition, the proximal boundary of the m2 region was set at the line to which a distance from the u/m border was 2 mm. Accordingly, longitudinal length of the m2 region was 1mm. Thus, the boundary between the m1 and m2 regions and the proximal boundary of the m2 region were strictly defined. Additionally, the division scheme used in the present study was systematically organized in the myelinated region.

Kawano (2015) described that GFAP immunoreactivity in the m1* region was stronger than that in the m2* region with a significant difference. Results obtained were compatible with these findings. Kawano (2015) also described that GS immunoreactivity in the m1* region was stronger than that in the m2* region, however, no significant difference was observed in the strength of GS immunoreactivity between the m1* and m2* regions. The present study confirmed the distribution pattern of GS immunoreactivity in the m1* and m2* regions, and reported that significant difference was observed in the strength of GS immunoreactivity between the m1ab and m2ab regions, between the m1ab and m2cd regions, between the m1cd and m2ab regions, and between the m1cd and m2cd regions.

Kawano (2025) demonstrated the concentration of MBPh-immunoreactive particles in the distal-most part of the myelinated region. The present study confirmed these findings.

4.3 | Characteristics of results obtained

4.3.1 | Relationship between the intensity of GFAP immunoreactivity and that of GFAP-immunoreactive filaments

The intensity of GFAP immunoreactivity was significantly strong in the m1ab region, moderate in the m1cd region, and weak in both the m2ab and m2cd regions (FIGURE 7A). This diversity was attributable to the significant differences in the proportion of total area of GFAP-immunoreactive filaments (astrocytic filaments): the proportion was significantly high in the m1ab region, moderate in the m1cd region, and low in both the m2ab and m2cd regions (FIGURE 7C). This notion was supported by the fact that there was no significant difference in the intensity of GFAP immunoreactivity in GFAP-immunoreactive filaments among the m1ab, m1cd, m2ab, and m2cd regions (FIGURE 7B).

4.3.2 | Relationship between the intensity of GS immunoreactivity and that of GS-immunoreactive cells

In the m1 and m2 regions, the intensity of GS immunoreactivity was significantly strong in the m1ab region, moderate in the m1cd region, and weak in both the m2ab and m2cd regions (FIGURE 8A). These dissimilarities were attributable to the significant differences in the intensity of GS immunoreactivity in GS-immunoreactive cells: the intensity was strong in the m1ab region, and moderate in the m1cd, m2ab, and m2cd regions (FIGURE 8B). The dissimilarities were also attributed by the significant differences in the proportion of total area of GS-immunoreactive cells: the proportion was large in the m1ab region, and medium in both the m2ab and m2cd regions (FIGURE 8C).

In the m1 region, the intensity of GS immunoreactivity was the strongest in the m1a region, moderate in the m1b region, and the weakest in both the m1c and m1d regions with significant differences (FIGURE 8F). This diversity was attributable to the significant differences in the intensity of GS immunoreactivity in GS-immunoreactive cells: the intensity was significantly strong in the m1a region, and moderate in both the m1c and m1d regions (FIGURE 8G). It is possible that this diversity was also attributed by the proportion of total

area of GS-immunoreactive cells, since four out of five proportions in each region were less than 1.00 from the m1b region through the m1d region, and since the median of the proportion in each region was approximately 0.7 from the m1b region through the m1d region: m1b, 0.72; m1c, 0.70; m1d, 0.72 (FIGURE 8H).

4.3.3 | Relationship between the intensity of bBM-labeling and that of bBM-labeled cell nuclei

The intensity of bBM-labeling was significantly strong in the m1ab region, and moderate in the m1cd, m2ab, and m2cd regions (FIGURE 9A). This dissimilarity was largely attributable to the significant differences in the proportion of total area of bBM-labeled cell nuclei: the proportion was large in the m1ab region, and moderate in the m1cd, m2ab and m2cd regions (FIGURE 9C). This notion was supported by the fact that there was no significant difference in the intensity of bBM-labeling in bBM-labeled cell nuclei among the m1ab, m1cd, and m2ab regions (FIGURE 9B).

In addition, the diversity of the proportion (of total area of bBM-labeled cell nuclei) was attributed by the significant differences in the density of bBM-labeled cell nuclei: the density was significantly high in the m1ab region, and medium in the m1cd, m2ab and m2cd regions (FIGURE 9D). This notion was strengthened by the fact that there was no significant difference in the mean area of bBM-labeled cell nuclei among the m1ab, m1cd, m2ab, and m2cd regions (FIGURE 9E).

4.3.4 | The intensity of MBPh immunoreactivity, and MBPh-immunoreactive particles related measurement value including shape descriptors of those

There were significant differences in five measurement values of MBPh-immunoreactive particles between the m1ab region and the other three regions: the m1cd,

m2ab, and m2cd regions. The five measurement values were as follows: the intensity of MBPh immunoreactivity in MBPh-immunoreactive particles, the proportion of total area of the particles, the density, the mean area, and the mean perimeter of the particles. Out of these five measurement values of MBPh-immunoreactive particles, the proportion of total area, and the density of those showed marked differences between the m1ab and the other three regions: the m1cd, m2ab, and m2cd regions. The diversity of the proportion was attributable to that in the density. This notion was supported by the fact that the differences in the mean area of those were minor between the m1ab region and the other three regions, although there were significant differences in the mean area of those between the m1ab and the m1cd regions, and between the m1ab and the m2ab regions.

On the other hand, there was no significant difference in the intensity of MBPh immunoreactivity among the m1ab, m1cd, m2ab, and m2cd regions. Thus, the dissimilarity of the five measurements values of MBPh-immunoreactive particles did not influence on the stability of intensity of MBPh immunoreactivity from the m1ab region through the m2cd region.

Shape descriptors of MBPh-immunoreactive particles were primarily stable from the m1ab region through the m2cd region except for the circularity and the roundness (FIGURE 11A-D). The roundness was significantly smaller in the m1ab region than that in the m1cd region (FIGURE 11C). However, this evidence was not supported by the fact that there was no significant difference in the roundness among the m1a, m1b, m1c, and m1d regions (FIGURE 11G). As for the circularity in the m1 region, it was significantly smaller in the m1ab region than that in the m1cd region (FIGURE 11A). Reliability of this evidence was strengthened by the fact that the circularity was significantly smaller in the m1a region than that in the m1d region (FIGURE 11E). Thus, shape descriptors of MBPh-immunoreactive

particles were primarily stable from the m1ab region through the m2cd region except for the circularity in the m1 region.

4.4 | Comparisons between the accumulation of GFAP-immunoreactive filaments in the m1ab region and astrogliosis

In this section, we discuss factors to induce the accumulation of the GFAP-immunoreactive filaments in the m1ab region. In this case, astrogliosis is useful for comparisons with the accumulation. Astrogliosis is a fibrous proliferation of glial cells in injured areas of the central nervous system (CNS; McAteer and Choudhury, 2009). Almost all brain lesions have a component of astrogliosis, even with different glial pathologies. Astrogliosis is a secondary event to damage in the CNS and may persist for weeks or months after brain injury. This condition occurs after infarct and is associated with infections and neoplasm as well as with demyelinating, toxic, and metabolic diseases. In astrogliosis, astrocytes hypertrophy, the nuclei become enlarged, and the chromatin becomes less dense while nucleoli become more prominent. There is an increased number of organelles and higher production of the intermediate filaments GFAP, nestin, and vimentin, which results in greater and more highly condensed glial processes and fibers (Messam et al., 2002). In addition, proliferation of astrocytes is seen in severe diffuse reactive astrogliosis (Sofroniew, 2013). Thus, higher production of GFAP is observed not only in astrogliosis but also in the m1ab region where GFAP-immunoreactive filaments were accumulated. Since astrogliosis is a secondary event to CNS damage, it is possible that the accumulation of GFAP-immunoreactive filaments in the m1ab region is attributable to mild histological damage in this region.

In astrogliosis, the nuclei of astrocytes become enlarged (Messam et al., 2002). In the present study, the mean area of bBM-labeled cell nuclei in the m1ab region was similar to

the other three myelinated regions: the m1cd, m2ab, and m2cd regions (FIGURE 9E). Since these cell nuclei were not only parts of astrocytes but also those of oligodendrocytes, microglia, endothelial cells, and of pericytes (Robison et al., 1989; Bron et al., 1997), there is a slight possibility that mean area of astrocyte nuclei is larger in the m1ab region than in the other three regions. Additionally, the proliferation of astrocytes is seen in severe diffuse reactive astrogliosis (Sofroniew, 2013). In the present study, the density of bBM-labeled cell nuclei was significantly higher in the m1ab region than in the other three regions. There is a distinct possibility that this diversity of the density is attributable to the higher density of astrocyte nuclei in the m1ab region. This notion is supported by the two facts. One is that majority (88-98%) of GS-immunoreactive cells are oligodendrocyte in the rat optic nerve (Kawano, 2015). Another is that the density of GS-immunoreactive cells in the m1ab region was similar to that in the other three regions (FIGURE 8D). In order to improve our notion that the rat has suffered mild histological damage to the m1ab region, further studies are required to clarify both the area of astrocyte nuclei and the density of those in the m1ab region and in the other three regions.

4.5 | Relationship between strong GS immunoreactivity in oligodendrocytes distributed in the m1ab region and a mildly pathological condition

GS expression in oligodendrocytes is increased in chronic pathological conditions in the mouse. The mouse in these conditions shows a significant increase in the number of GS-immunoreactive cell bodies as well as a tendency for increased GS immunoreactivity per oligodendrocytes at end-stage as compared to controls (Ben Haim et al., 2021). In the present study, the density of GS-immunoreactive cells was largely constant from the m1ab region through the m2cd region. However, a significant increase in GS immunoreactivity was observed in GS-immunoreactive cells of the m1ab region as compared to those of the other

three regions: m1cd, m2ab, and m2cd regions. Accordingly, it is possible that the significant increase in GS immunoreactivity of GS-immunoreactive cells in the m1ab region is attributable to not a physiological but a pathological condition in this region.

This interpretation is also supported by evidence relating axo-myelinic neurotransmission and oligodendrocyte myelination. In the physiological state, the myelination of axons by oligodendrocytes in a highly complex cell-to-cell interaction. Oligodendrocytes and axons have a reciprocal signaling relationship (axo-myelinic neurotransmission) in which oligodendrocytes receive cues from axons that direct their myelination, and oligodendrocytes subsequently shape axonal structure and conduction (oligodendrocyte myelination; Duncan et al., 2021). As for axo-myelinic neurotransmission in the rat optic nerve, the glutamate is a key signaling factor (Barron and Kim, 2019), since retino-geniculate neurons are glutamatergic (Salt, 1986; Kielland and Heggelund, 2002; Govindaiah et al., 2012). During propagation of action potentials, traversing action potentials cause depolarization of the axon. The depolarization is sensed by voltage-gated Ca^{2+} channels, which in turn activate and cause intra-axonal Ca^{2+} release from the axoplasmic reticulum. This stimulates the fusion of glutamatergic vesicles and the consequent release of glutamate into the peri-axonal space, which in turn activate myelinic AMPA and NMDA receptors, located on the innermost myelin sheaths, finally promoting Ca^{2+} influx into the myelin cytoplasm (Micu et al., 2016; Micu et al., 2018; Barron and Kim, 2019; Bergaglio et al., 2021; Duncan et al., 2021). The Ca^{2+} influx is able to lead to various downstream Ca^{2+} pathways important for myelination and oligodendrocyte function (Barron and Kim, 2019). Glutamate in the peri-axonal space is then likely taken up by glutamate transporters on axons for reloading into vesicles (Micu et al., 2018), and by those on oligodendrocytes for transforming glutamate into glutamine by using GS, since majority of GS-immunoreactive cells are oligodendrocytes in the rat optic nerve (Kawano, 2015).

In the pathological state, excessive vesicular glutamate release into the peri-axonal space is proposed (Micu et al., 2018; Bergaglio et al., 2021). Accordingly, glutamate clearance is required in this space in order to prevent excitotoxicity induced by immoderate glutamate accumulation. To clear immoderate glutamate in the peri-axonal space, glutamate is taken up by using glutamate transporters on axons for reloading into vesicles, and by those on oligodendrocytes for transforming glutamate into glutamine by GS. Since a large quantity of glutamate is taken into these cells, GS expression is increased in these oligodendrocytes. Thus, it is possible that the significant increase in GS immunoreactivity of GS-immunoreactive cells in the m1ab region is attributable to not a physiological but a pathological condition in this region.

4.6 | Relationship between myelin debris-like MBPh-immunoreactive particles distributed in the m1ab region and the mildly pathological condition

Density of MBPh-immunoreactive particles was high in the m1ab region (FIGURE 10D), especially in the m1a region (FIGURE 10J). Immunohistochemical characteristics of these MBP-immunoreactive particles were similar to those of myelin debris. This notion was supported by the following three facts. First, not only MBPh-immunoreactive particles but also myelin debris were immunoreactive for myelin basic protein (MBP). Second, similar to the distribution of myelin debris, MBPh-immunoreactive particles were located on or around myelinated nerve fibers (present study, Kawano, 2025). Third, the size and shape of MBPh-immunoreactive particles were similar to those of myelin debris (Kawano, 2025). In addition to these facts, a considerable amount of myelin debris has been observed in pathological condition (Weinger et al, 2011; Zhou et al., 2019; Wang et al., 2020; Yao et al, 2023). Therefore, it is probable that the m1a (m1ab) region was under mildly pathological condition, since this region was rich in myelin debris-like MBPh-immunoreactive particles.

It has been reported that myelin debris is cleared by microglia and/or monocyte-derived macrophages in pathological condition (Stoll et al, 1989; Stoll and Jander, 1999; Weinger et al, 2011; Lloyd et al, 2017; Hammel et al., 2022). Recent studies demonstrated that astrocytes (Wang et al., 2020; Hammel et al., 2022; Li et al., 2023) and microvascular endothelial cells (Zhou et al., 2019; Hammel et al., 2022; Yao et al., 2023) also clear myelin debris. These findings suggest that not only microglia and/or monocyte-derived macrophages but also astrocytes and microvascular endothelial cells phagocytose myelin debris-like MBPh-immunoreactive particles distributed in the m1a (m1ab) region of the normal rat optic nerve. Further studies are required to clarify whether this notion is appropriate or not.

In addition to the phagocytosis of myelin debris by microglia and/or by other phagocytes in pathological condition, it has been demonstrated that myelin debris causes the inflammatory response. For example, direct application of myelin debris into the corpus callosum or the cerebral cortex induces profound and comparable inflammation in these structures of the mouse (Clarner et al., 2012; Grajchen et al., 2020; Hammel et al., 2022). It is possible that myelin debris-like MBPh-immunoreactive particles might also induce the inflammatory response in the m1a (m1ab) region of the normal rat optic nerve. Further studies are needed to elucidate whether this notion is appropriate or not.

4.7 | The mildly pathological condition in the m1a (m1ab) region

The myelinated region of the normal rat optic nerve had been recognized to be homogeneously organized. Kawano (2015) demonstrated that the chemoarchitecture of the myelinated region was heterogeneously organized. In the present study, we confirmed the previous findings and proposed a notion that the heterogeneous distribution of the two glial cell marker proteins (GFAP, and GS) and of MBPh-immunoreactive particles in the

myelinated region was attributable to the mildly pathological condition in the m1a (m1ab) region of the normal rat optic nerve.

In spite of the fact that the m1a (m1ab) region is a part of the normal rat optic nerve, it is not known why this region is under the mildly pathological condition. One possible background to induce this condition is that the m1a (m1ab) region is located next to the u (unmyelinated) region. The u region is one of the strongest regions of GFAP immunoreactivity (Kawano, 2015). Accordingly, the u region shows a necessary requirement of gliosis: higher production of GFAP. In addition, gliosis in the u region might be severe because of the strongest GFAP immunoreactivity in this region. With astrogliosis there is the release of cytokines, growth factors, and extracellular matrix proteins that may be involved in immune response, neuroprotection, or possible further damage (Messam et al, 2002). It is possible that there is the release of these bioactive chemicals in the u region and that these released bioactive chemicals are spread into the m1a (m1ab) region. Thus, the m1a (m1ab) region might be impaired not only by the released bioactive chemicals in the same region due to astrogliosis but also by those from the next (u; unmyelinated) region.

This interpretation is supported by the fact that the capillary bed (Morrison et al., 1999; Sugiyama et al., 1999) is located in the proximal (posterior) half of the u region (Kawano, 2015). The present study shows defects in GFAP immunoreactivity (FIGURE 1B) and those in GS immunoreactivity (FIGURE 2B) in this region. Since the capillary bed allows more nutrients and oxygens to enrich the tissue, thereby providing a healthier environment (Erickson and Liu-Ambrose, 2016), it is supposed that the capillary bed is required in this region in order to prevent the impairment of tissue by the released bioactive chemicals.

4.8 | Conclusion

In summary, GFAP and GS were distributed abundantly in the m1ab region, moderately in the m1cd region, and sparsely in the m2ab and m2cd regions. In addition, bBM-labeled cell nuclei were present plentifully in the m1ab region, and moderately in the m1cd, m2ab, and m2cd regions. Interestingly, MBPh-immunoreactive particles were distributed abundantly in the m1ab region, but sparsely in the m1cd, m2ab and m2cd regions.

Since astrogliosis is a fibrous proliferation of glial cells in injured areas of the CNS, abundant distribution of GFAP in the m1ab region suggests that the m1ab region might be under the mildly pathological condition (McAteer and Choudhury, 2009). Since GS in oligodendrocytes is increased in chronic pathological conditions in mice and humans, abundant distribution of GS in the m1ab region indicates that the m1ab region is under the mildly pathological condition (Ben Haim et al., 2021). Since MBPh-immunoreactive particles are considered to be myelin debris-like structures, abundant distribution of these particles in the m1ab region suggests that the m1ab region might be under the mildly pathological condition (Kawano, 2025). Consequently, concentration of GFAP, GS, cell nuclei, and of MBP-immunoreactive particles in the m1ab region might be a significant functional adjustment that indicates the not physiological but mildly pathological nature of the structural environment of this part in the normal rat optic nerve.

Further studies on optic nerve glutamate homeostasis are needed in the m1ab region, that is not in physiological (healthy) but in mildly pathological (diseased) states. These studies will increase our fundamental understanding of the optic nerve and may provide new insight into several optic nerve diseases.

Author Contributions

J.K.: Concept, Funding, Supervision, Investigation, Data analysis, Writing original draft, Writing – review and editing.

Acknowledgments

The author thanks Professor Masahisa Horiuchi (Department of Hygiene and Health Promotion Medicine, Kagoshima University Graduate School of Medical and Dental Sciences) for his expert advice on statistical analyses. This work was supported by an annual fund from Kagoshima University.

Conflicts of Interest

The author declares no conflicts of interest.

Data Availability Statement

The data that support the findings of this study are available from the corresponding author upon reasonable request.

REFERENCES

Balaratnasingam, C., Kang, M. H., Yu, P., Chan, G., Morgan, W. H., Cringle, S. J., & Yu, D. Y. (2014). Comparative quantitative study of astrocytes and capillary distribution in optic nerve laminar regions. *Experimental Eye Research, 121*, 11-22. https://doi.org/10.1016/j.exer.2014.02.008

Balaratnasingam, C., Morgan, W. H., Johnstone, V., Cringle, S. J., & Yu, D. Y. (2009). Heterogeneous distribution of axonal cytoskeleton proteins in the human optic nerve. *Investigative Ophthalmology & Visual Science, 50*(6), 2824-2838. https://doi.org/10.1167/iovs.08-3206

Barron, T., & Kim, J. H. (2019). Neuronal input triggers Ca^{2+} influx through AMPA receptors and voltage-gated Ca^{2+} channels in oligodendrocytes. *Glia, 67*(10), 1922-1932. https://doi.org/10.1002/glia.23670

Ben Haim, L., Schirmer, L., Zulji, A., Sabeur, K., Tiret, B., Ribon, M., Chang, S., Lamers, W. H., Boillée, S., Chaumeil, M. M., & Rowitch, D. H. (2021). Evidence for glutamine synthetase function in mouse spinal cord oligodendrocytes. *Glia, 69*(12), 2812-2827. https://doi.org/10.1002/glia.24071

Bergaglio, T., Luchicchi, A., & Schenk, G. J. (2021). Engine Failure in Axo-Myelinic Signaling: A Potential Key Player in the Pathogenesis of Multiple Sclerosis. *Frontiers in Cellular Neuroscience, 15*, 610295. https://doi.org/10.3389/fncel.2021.610295

Black, J. A., Waxman, S. G., & Hildebrand, C. (1985). Axo-glial relations in the retina-optic nerve junction of the adult rat: freeze-fracture observations on axon membrane structure. *Journal of Neurocytology, 14*(6), 887-907. https://doi.org/10.1007/BF01224803

Bron, A. J., Tripathi, R. C., & Tripathi, B. J. (1997). The Visual Pathway. In: A. J. Bron, R. C. Tripathi, & B. J. Tripathi (Eds.), *Wolff's Anatomy of the Eye and Orbit.* (8th ed., pp. 489-596). London: Chapman & Hall.

Chang, M. L., Wu, C. H., Jiang-Shieh, Y. F., Shieh, J. Y., & Wen, C. Y. (2007). Reactive changes of retinal astrocytes and Müller glial cells in kainate-induced neuroexcitotoxicity. *Journal of Anatomy, 210*(1), 54-65. https://doi.org/10.1111/j.1469-7580.2006.00671.x

Clarner, T., Diederichs, F., Berger, K., Denecke, B., Gan, L., van der Valk, P., Beyer, C., Amor, S., & Kipp, M. (2012). Myelin debris regulates inflammatory responses in an experimental demyelination animal model and multiple sclerosis lesions. *Glia, 60*(10), 1468-1480. https://doi.org/10.1002/glia.22367

Darman, J., Backovic, S., Dike, S., Maragakis, N. J., Krishnan, C., Rothstein, J. D., Irani, D. N., & Kerr, D. A. (2004). Viral-induced spinal motor neuron death is non-cell-autonomous and involves glutamate excitotoxicity. *Journal of Neuroscience, 24*(34), 7566-7575. https://doi.org/10.1523/JNEUROSCI.2002-04.2004

Duncan, G. J., Simkins, T. J., & Emery, B. (2021). Neuron-Oligodendrocyte Interactions in the Structure and Integrity of Axons. *Frontiers in Cell and Developmental Biology, 9*, 653101. https://doi.org/10.3389/fcell.2021.653101

Dyer, C. A., Kendler, A., Philibotte, T., Gardiner, P., Cruz, J., & Levy, H. L. (1996). Evidence for central nervous system glial cell plasticity in phenylketonuria. *Journal of Neuropathology & Experimental Neurology, 55*(7), 795-814. https://doi.org/10.1097/00005072-199607000-00005

Erickson, K. I., & Liu-Ambrose, T. (2016). Exercise, Cognition, and Health. In K. W. Schaie & S. L. Willis (Eds.), *Handbook of the Psychology of Aging* (8th ed., pp. 187-201). San Diego: Academic Press. https://doi.org/10.1016/B978-0-12-411469-2.00010-8

Ffrench-Constant, C., Miller, R. H., Burne, J. F., & Raff, M. C. (1988). Evidence that

migratory oligodendrocyte-type-2 astrocyte (O-2A) progenitor cells are kept out of the rat retina by a barrier at the eye-end of the optic nerve. *Journal of Neurocytology, 17*(1), 13-25. https://doi.org/10.1007/BF01735374

Fox, J. (2017). *Using the R commander, A Point-and-Click Interface for R* (1st ed.). Boca Raton, Florida: Chapman and Hall/CRC Press. https://doi.org/10.1201/9781315380537

Friedman, B., Hockfield, S., Black, J. A., Woodruff, K. A., & Waxman, S. G. (1989). In situ demonstration of mature oligodendrocytes and their processes: An immunocytochemical study with a new monoclonal antibody, Rip. *Glia, 2*(5), 380-390. https://doi.org/10.1002/glia.440020510

Goldstein, M. E., Sternberger, L. A., & Sternberger, N. H. (1983). Microheterogeneity ("neurotypy") of neurofilament proteins. *Proceedings of the National Academy of Sciences of the United States of America, 80*(10), 3101-3105. https://doi.org/10.1073/pnas.80.10.3101

Goldstein, M. E., Sternberger, L. A., & Sternberger, N. H. (1987). Varying degrees of phosphorylation determine microheterogeneity of the heavy neurofilament polypeptide (Nf-H). *Journal of Neuroimmunology, 14*(2), 135-148. https://doi.org/10.1016/0165-5728(87)90048-8

Govindaiah, G., Wang, T., Gillette, M. U., & Cox, C. L. (2012). Activity-dependent regulation of retinogeniculate signaling by metabotropic glutamate receptors. *Journal of Neuroscience, 32*(37), 12820-12831. https://doi.org/10.1523/jneurosci.0687-12.2012

Grajchen, E., Wouters, E., van de Haterd, B., Haidar, M., Hardonnière, K., Dierckx, T., Van Broeckhoven, J., Erens, C., Hendrix, S., Kerdine-Römer, S., Hendriks, J. J. A., & Bogie, J. F. J. (2020). CD36-mediated uptake of myelin debris by macrophages and microglia reduces neuroinflammation. *Journal of Neuroinflammation, 17*(1), 224. https://doi.org/10.1186/s12974-020-01899-x

Hammel, G., Zivkovic, S., Ayazi, M., & Ren, Y. (2022). Consequences and mechanisms of myelin debris uptake and processing by cells in the central nervous system. *Cellular Immunology, 380*, 104591. https://doi.org/10.1016/j.cellimm.2022.104591

Haverkamp, S., & Wässle, H. (2000). Immunocytochemical analysis of the mouse retina. *The Journal of Comparative Neurology, 424*(1), 1-23. https://doi.org/10.1002/1096-9861(20000814)424:1<1::AID-CNE1>3.0.CO;2-V

Hojo, M., Ohtsuka, T., Hashimoto, N., Gradwohl, G., Guillemot, F., & Kageyama, R. (2000). Glial cell fate specification modulated by the bHLH gene *Hes5* in mouse retina. *Development, 127*(12), 2515-2522. https://doi.org/10.1242/dev.127.12.2515

Howell, G. R., Libby, R. T., Jakobs, T. C., Smith, R. S., Phalan, F. C., Barter, J. W., Barbay, J. M., Marchant, J. K., Mahesh, N., Porciatti, V., Whitmore, A. V., Masland, R. H., & John, S. W. (2007). Axons of retinal ganglion cells are insulted in the optic nerve early in DBA/2J glaucoma. *Journal of Cell Biology, 179*(7), 1523-1537. https://doi.org/10.1083/jcb.200706181

Jalil, M. A., Begum, L., Contreras, L., Pardo, B., Iijima, M., Li, M. X., Ramos, M., Marmol, P., Horiuchi, M., Shimotsu, K., Nakagawa, S., Okubo, A., Sameshima, M., Isashiki, Y., del Arco, A., Kobayashi, K., Satrústegui, J., & Saheki, T. (2005). Reduced N-acetylaspartate levels in mice lacking aralar, a brain- and muscle-type mitochondrial aspartate-glutamate carrier. *Journal of Biological Chemistry, 280*(35), 31333-31339. https://doi.org/10.1074/jbc.M505286200

Ju, W. K., Misaka, T., Kushnareva, Y., Nakagomi, S., Agarwal, N., Kubo, Y., Lipton, S. A., & Bossy-Wetzel, E. (2005). OPA1 expression in the normal rat retina and optic nerve. *The Journal of Comparative Neurology, 488*(1), 1-10.

https://doi.org/10.1002/cne.20586
Kanda, Y. (2013). Investigation of the freely available easy-to-use software 'EZR' for medical statistics. *Bone Marrow Transplantation, 48*(3), 452-458. https://doi.org/10.1038/bmt.2012.244
Kawano, J. (2015). Chemoarchitecture of glial fibrillary acidic protein (GFAP) and glutamine synthetase in the rat optic nerve: An immunohistochemical study. *Okajimas Folia Anatomica Japonica, 92*(1), 11-30. https://doi.org/10.2535/ofaj.92.11
Kawano, J. (2025). Concentration of myelin debris-like myelin basic protein-immunoreactive particles in the distal (anterior)-most part of the myelinated region in the normal rat optic nerve. *bioRxiv,* Submitted.
Kawano, J., Tanizawa, Y., & Shinoda, K. (2008). Wolfram syndrome 1 (*Wfs1*) gene expression in the normal mouse visual system. *The Journal of Comparative Neurology, 510*(1), 1-23. https://doi.org/10.1002/cne.21734
Khakh, B. S., & Deneen, B. (2019). The Emerging Nature of Astrocyte Diversity. *Annual Review of Neuroscience, 42*, 187-207. https://doi.org/10.1146/annurev-neuro-070918-050443
Kielland, A., & Heggelund, P. (2002). AMPA and NMDA currents show different short-term depression in the dorsal lateral geniculate nucleus of the rat. *The Journal of Physiology, 542*(Pt 1), 99-106. https://doi.org/10.1113/jphysiol.2002.019240
Li, X., Ding, Z., Liu, K., Wang, Q., Song, L., Chai, Z., Yu, J., Ma, D., Xiao, B., & Ma, C. (2023). Astrocytic phagocytosis of myelin debris and reactive characteristics in vivo and in vitro. *Biology of the Cell, 115*(12), e202300057. https://doi.org/10.1111/boc.202300057
Lloyd, A. F., Davies, C. L., & Miron, V. E. (2017). Microglia: origins, homeostasis, and roles in myelin repair. *Current Opinion in Neurobiology, 47*, 113-120. https://doi.org/10.1016/j.conb.2017.10.001
May, C. A. (2003). The optic nerve head region of the aged rat: An immunohistochemical investigation. *Current Eye Research, 26*(6), 347-354. https://doi.org/10.1076/ceyr.26.5.347.15438
McAteer, M. A., & Choudhury, R. P. (2009). Applications of nanotechnology in molecular imaging of the brain. *Progress in Brain Research, 180*, 72-96. https://doi.org/10.1016/s0079-6123(08)80004-0
Melo, P., Moreno, V. Z., Vázquez, S. P., Pinazo-Durán, M. D., & Tavares, M. A. (2006). Myelination changes in the rat optic nerve after prenatal exposure to methamphetamine. *Brain Res, 1106*(1), 21-29. https://doi.org/10.1016/j.brainres.2006.05.020
Messam, C., Hou, J., Janabi, N., Monaco, M., Gravell, M., & Major, E. (2002). Glial cell types. In V. S. Ramachandran (Ed.), *Encyclopedia of the Human Brain* (1st ed., Vol. 2, pp. 369-387). San Diego: Academic Press. https://doi.org/10.1016/B0-12-227210-2/00152-7
Micu, I., Plemel, J. R., Caprariello, A. V., Nave, K.-A., & Stys, P. K. (2018). Axo-myelinic neurotransmission: a novel mode of cell signalling in the central nervous system. *Nature Reviews Neuroscience, 19*(1), 49-58. https://doi.org/10.1038/nrn.2017.128
Micu, I., Plemel, J. R., Lachance, C., Proft, J., Jansen, A. J., Cummins, K., van Minnen, J., & Stys, P. K. (2016). The molecular physiology of the axo-myelinic synapse. *Experimental Neurology, 276*, 41-50. https://doi.org/10.1016/j.expneurol.2015.10.006
Morcos, Y., & Chan-Ling, T. (2000). Concentration of astrocytic filaments at the retinal optic nerve junction is coincident with the absence of intra-retinal myelination: comparative and developmental evidence. *Journal of Neurocytology, 29*(9), 665-678. https://doi.org/10.1023/A:1010835404754

Morrison, J. C., Johnson, E. C., Cepurna, W. O., & Funk, R. H. W. (1999). Microvasculature of the rat optic nerve head. *Investigative Ophthalmology & Visual Science, 40*(8), 1702-1709.

Morrison, J. C., Johnson, E. C., Cepurna, W., & Jia, L. (2005). Understanding mechanisms of pressure-induced optic nerve damage. *Progress in Retinal and Eye Research, 24*(2), 217-240. https://doi.org/10.1016/j.preteyeres.2004.08.003

Riepe, R. E., & Norenburg, M. D. (1977). Müller cell localisation of glutamine synthetase in rat retina. *Nature, 268*(5621), 654-655. https://doi.org/10.1038/268654a0

Robison, W. G., Jr., Nagata, M., Tillis, T. N., Laver, N., & Kinoshita, J. H. (1989). Aldose reductase and pericyte-endothelial cell contacts in retina and optic nerve. *Investigative Ophthalmology & Visual Science, 30*(11), 2293-2299.

Saari, J. C., Huang, J., Possin, D. E., Fariss, R. N., Leonard, J., Garwin, G. G., Crabb, J. W., & Milam, A. H. (1997). Cellular retinaldehyde-binding protein is expressed by oligodendrocytes in optic nerve and brain. *Glia, 21*(3), 259-268. https://doi.org/10.1002/(SICI)1098-1136(199711)21:3<259::AID-GLIA1>3.0.CO;2-0

Salt, T. E. (1986). Mediation of thalamic sensory input by both NMDA receptors and non-NMDA receptors. *Nature, 322*(6076), 263-265. http://doi.org/10.1038/322263a0

Serwanski, D. R., Jukkola, P., & Nishiyama, A. (2017). Heterogeneity of Astrocyte and NG2 Cell Insertion at the Node of Ranvier. *The Journal of Comparative Neurology, 525*(3), 535-552. https://doi.org/10.1002/cne.24083

Sofroniew, M. V. (2013). Astrocyte responses to central nervous system injury and disease. In H. Kettenmann & B. R. Ransom (Eds.), *Neuroglia* (3rd ed., pp. 653-664). New York: Oxford University Press. https://doi.org/10.1093/med/9780199794591.003.0051

Sternberger, L. A., & Sternberger, N. H. (1983). Monoclonal antibodies distinguish phosphorylated and nonphosphorylated forms of neurofilaments *in situ*. *Proceedings of the National Academy of Sciences of the United States of America, 80*(19), 6126-6130. https://doi.org/10.1073/pnas.80.19.6126

Sternberger, L. A., Harwell, L. W., & Sternberger, N. H. (1982). Neurotypy: regional individuality in rat brain detected by immunocytochemistry with monoclonal antibodies. *Proceedings of the National Academy of Sciences of the United States of America, 79*(4), 1326-1330. https://doi.org/10.1073/pnas.79.4.1326

Stoll, G., & Jander, S. (1999). The role of microglia and macrophages in the pathophysiology of the CNS. *Progress in Neurobiology, 58*(3), 233-247. https://doi.org/10.1016/s0301-0082(98)00083-5

Stoll, G., Trapp, B. D., & Griffin, J. W. (1989). Macrophage function during Wallerian degeneration of rat optic nerve: clearance of degenerating myelin and Ia expression. *Journal of Neuroscience, 9*(7), 2327-2335. https://doi.org/10.1523/jneurosci.09-07-02327.1989

Sugiyama, K., Gu, Z.-B., Kawase, C., Yamamoto, T., & Kitazawa, Y. (1999). Optic nerve and peripapillary choroidal microvasculature of the rat eye. *Investigative Ophthalmology & Visual Science, 40*(13), 3084-3090.

Sun, D., Lye-Barthel, M., Masland, R. H., & Jakobs, T. C. (2009). The Morphology and Spatial Arrangement of Astrocytes in the Optic Nerve Head of the Mouse. *The Journal of Comparative Neurology, 516*(1), 1-19. https://doi.org/10.1002/cne.22058

Talos, D. M., Fishman, R. E., Park, H., Folkerth, R. D., Follett, P. L., Volpe, J. J., & Jensen, F. E. (2006). Developmental regulation of α-amino-3-hydroxy-5-methyl-4-isoxazole-propionic acid receptor subunit expression in forebrain and relationship to regional susceptibility to hypoxic/ischemic injury. I. Rodent cerebral white matter and cortex. *The Journal of Comparative Neurology, 497*(1), 42-60.

https://doi.org/10.1002/cne.20972

Wang, S., Deng, J., Fu, H., Guo, Z., Zhang, L., & Tang, P. (2020). Astrocytes directly clear myelin debris through endocytosis pathways and followed by excessive gliosis after spinal cord injury. *Biochemical and Biophysical Research Communications, 525*(1), 20-26. https://doi.org/10.1016/j.bbrc.2020.02.069

Warr, W. B., de Olmos, J. S., & Heimer, L. (1981). Horseradish Peroxidase: The Basic Procedure. In L. Heimer & M. J. Robards (Eds.), *Neuroanatomical tract-tracing methods.* (1st ed., pp. 207-262). New York: Plenum Press. https://doi.org/10.1007/978-1-4613-3189-6_6

Weinger, J. G., Brosnan, C. F., Loudig, O., Goldberg, M. F., Macian, F., Arnett, H. A., Prieto, A. L., Tsiperson, V., & Shafit-Zagardo, B. (2011). Loss of the receptor tyrosine kinase Axl leads to enhanced inflammation in the CNS and delayed removal of myelin debris during Experimental Autoimmune Encephalomyelitis. *Journal of Neuroinflammation, 8*, 49. https://doi.org/10.1186/1742-2094-8-49

Yao, F., Luo, Y., Chen, Y., Li, Y., Hu, X., You, X., Li, Z., Yu, S., Tian, D., Zheng, M., Cheng, L., & Jing, J. (2023). Myelin Debris Impairs Tight Junctions and Promotes the Migration of Microvascular Endothelial Cells in the Injured Spinal Cord. *Cellular and Molecular Neurobiology, 43*(2), 741-756. https://doi.org/10.1007/s10571-022-01203-w

Yazdankhah, M., Shang, P., Ghosh, S., Hose, S., Liu, H., Weiss, J., Fitting, C. S., Bhutto, I. A., Zigler, J. S., Jr., Qian, J., Sahel, J. A., Sinha, D., & Stepicheva, N. A. (2021). Role of glia in optic nerve. *Progress in Retinal and Eye Research, 81*, 100886. https://doi.org/10.1016/j.preteyeres.2020.100886

Zabouri, N., Bouchard, J.-F., & Casanova, C. (2011). Cannabinoid receptor type 1 expression during postnatal development of the rat retina. *The Journal of Comparative Neurology, 519*(7), 1258-1280. https://doi.org/10.1002/cne.22534

Zhou, T., Zheng, Y., Sun, L., Badea, S. R., Jin, Y., Liu, Y., Rolfe, A. J., Sun, H., Wang, X., Cheng, Z., Huang, Z., Zhao, N., Sun, X., Li, J., Fan, J., Lee, C., Megraw, T. L., Wu, W., Wang, G., & Ren, Y. (2019). Microvascular endothelial cells engulf myelin debris and promote macrophage recruitment and fibrosis after neural injury. *Nature Neuroscience, 22*(3), 421-435. https://doi.org/10.1038/s41593-018-0324-9

Figure Legends

FIGURE 1 **A-B:** Distribution of astrocytes and oligodendrocytes in the normal rat optic nerve. The panels show a longitudinal section through the paramedian part, and represent double immunostaining for an astrocyte marker (glial fibrillary acidic protein, GFAP; B; Alexa Fluor 488 label; green in A) and an oligodendrocyte marker (RIP; Alexa Fluor 594 label; magenta in A). Cell nuclei were labeled with bisBenzimide (Hoechst 33258; blue in A). Panel A is an overlaid image. The arrows indicate the border between the unmyelinated (u) and myelinated regions. The double arrowheads represent boundaries between the subregions: the boundary between myelinated regions 1cd (m1cd) and 2ab (m2ab), or the boundary between myelinated regions 2cd (m2cd) and 3. The arrowheads show borders between the sub-subregions: the border between myelinated region 1ab (m1ab) and m1cd, or the border between m2ab and m2cd. Panel A is a photo montage composed of 10 square fluorescent images. These images were taken with an LSM 700 confocal microscope (Carl Zeiss, Jena, Germany). Parts of the background were filled up with a black color. Note that GFAP immunoreactivity in the m1ab region was stronger than that in the other three myelinated regions: the m1cd, m2ab, and m2cd regions. Interestingly, columns of astrocytes were seen to interdigitate with myelinated (RIP-immunoreactive) nerve fiber bundles in the m1ab region. i, intraretinal region; NFL, nerve fiber layer of the retina.

C: Diagram showing a division scheme in the rat optic nerve used in this study. In this diagram, shading demonstrates areas where quantitative analyses were performed. The optic nerve was divided into 6 regions: intraretinal (i) region, unmyelinated (u) region, and myelinated regions 1ab (m1ab), 1cd (m1cd), 2ab (m2ab), and 2cd (m2cd). The dashed lines made up of dashes and shorter gaps indicate the border between the u and m1ab regions. The dashed lines made up of dashes and longer gaps show the boundary between each subregion: for example, the boundary between the m1ab and m1cd regions, or the boundary between the

m1cd and m2ab regions. The one up-down arrow at the left of the m1ab region indicates that the longitudinal length of the m1ab region is 500 µm. The four up-down arrows at the right side of the m1ab, m1cd, m2ab, and m2cd regions, the lengths of which are the same, also show that the longitudinal length of each region is 500 µm. Note that the m1ab region was thicker than the other three myelinated regions: the m1cd, m2ab, and m2cd regions. NFL, nerve fiber layer of the retina.

D: Diagram showing another division scheme in the rat optic nerve used in this study. In this diagram, shading demonstrates areas where quantitative analyses were performed. The optic nerve was divided into 6 regions: intraretinal (i) region, unmyelinated (u) region, and myelinated regions 1a (m1a), 1b (m1b), 1c (m1c), and 1d (m1d). The dashed lines made up of dashes and shorter gaps indicate the border between the u and m1a regions. The dashed lines made up of dashes and longer gaps show the boundary between subregions: for example, the boundary between the m1a and m1b regions, or the boundary between the m1d region and myelinated region 2. The one up-down arrow at the left of the m1a region indicates that the longitudinal length of the m1a region is 250 µm. The four up-down arrows at the right side of the m1a, m1b, m1c, and m1d regions, the lengths of which are the same, also show that the longitudinal length of each region is 250 µm. NFL, nerve fiber layer of the retina. Scale bar = 200 µm for A-C.

FIGURE 2 Distribution of glutamine synthetase (GS)-immunoreactive glial cells, myelin basic protein (MBPh[3])-immunoreactive nerve fiber bundles, and of MBPh-

[3] In the companion pater (Kawano, 2025), we used two kinds of anti-myelin basic protein (MBP) antibodies which detect different positions of the MBP protein in order to analyze distribution of the MBP protein in the normal rat optic nerve: One was an antibody reacts

immunoreactive particles in the normal rat optic nerve. The panels show a longitudinal section through the paramedian part and represent double immunostaining for a glial cell marker (glutamine synthetase, GS; B; Alexa Fluor 488 label; green in A) and a myelin marker (myelin basic protein, MBPh; C; Alexa Fluor 594 label; magenta in A). Cell nuclei were labeled with bisBenzimide (Hoechst 33258; D; blue in A). Panel A is an overlaid image. The arrows indicate the border between the unmyelinated (u) region and myelinated region 1ab (m1ab). The double arrowheads represent boundaries between the subregions: the boundary between myelinated regions 1cd (m1cd) and 2ab (m2ab), or the boundary between myelinated regions 2cd (m2cd) and 3. The arrowheads show borders between the sub-subregions: the border between the m1ab and m1cd regions, or the border between the m2ab and m2cd regions. Panel A is a photo montage composed of 11 square fluorescent images. These images were taken with an LSM 700 confocal microscope (Carl Zeiss Jena, Germany). Parts of the background in panel A were filled up with a black color. Note that many MBPh-immunoreactive particles were distributed in the m1ab region, especially in the distal (anterior) half of the m1ab region. Interestingly, the distal half of the m1ab region was the major site for GS distribution in the normal rat optic nerve; however, GS immunoreactivity in this region was markedly weaker than that in the retina. NFL, nerve fiber layer of the retina. Scale bar = 200 μm in D for A-C.

---

with Ala-Ser-Asp-Tyr-Lys-Ser (ASDYKS) in position 131-136 of the classic human myelin basic protein (MBPh), another was an antibody reacts with Asp-Glu-Asn-Pro-Val-Val (DENPVV) in position 82-87 of the full length protein of the cow myelin basic protein (MBPc). Here we describe not MBP but MBPh to clarify which antibody was used to visualize the MBP protein.

FIGURE 3 **A-B:** Images used for quantitative analyses of glial fibrillary acidic protein (GFAP) distribution along the course of the myelinated regions of the normal rat optic nerve. The original image of FIGURE 1B, in which brightness and contrast were not adjusted (in which the brightness levels of an image histogram were not moved or stretched), was modified to create these images. Black background of the original image was removed manually on Adobe Photoshop CS5. The left edges of the m1ab (myelinated region 1ab) and m1a (myelinated region 1a) images indicate the border between the unmyelinated and myelinated regions. The horizontal length of each image is 500 µm in A and 250 µm in B. The background color of each modified image is complete white for the presentation.[4] The "Retina" and the "OX (optic chiasm)" show the orientation of each modified image. The scale in the bottom of each modified image represents a distance from the border between the unmyelinated and myelinated regions (Distance from u/m Border). **C:** The black binary image used to measure area of the m1a region. **D:** The white parts of this binary image indicate ROIs (regions of interest) to analyze mean pixel intensity of GFAP immunoreactivity, and proportion of total area of GFAP-immunoreactive filaments in the m1a region. m1b, myelinated region 1b; m1c, myelinated region 1c; m1cd, myelinated region 1cd; m1d, myelinated region 1d; m2ab, myelinated region 2ab; m2cd, myelinated region 2cd. Scale bar = 200 µm in D for A-C.

FIGURE 4 **A-B:** Images used for quantitative analyses of glutamine synthetase (GS) distribution along the course of the myelinated regions of the normal rat optic nerve. The original image of FIGURE 2B, in which brightness and contrast were not adjusted (in

[4] In our quantitative analyses, we used these modified images placed on the complete black background.

which the brightness levels of an image histogram were not moved or stretched), was modified to create these images. Black background of the original image was removed manually on Adobe Photoshop CS5. The left edges of the m1ab (myelinated region 1ab) and m1a (myelinated region 1a) images indicate the border between the unmyelinated and myelinated regions. The horizontal length of each image is 500 µm in A and 250 µm in B. The background color of each modified image is complete white for the presentation. The "Retina" and the "OX (optic chiasm)" show the orientation of each modified image. The scale in the bottom of each modified image represents a distance from the border between the unmyelinated and myelinated regions (Distance from u/m Border). **C:** The black binary image used to measure area of the m1a region. **D:** The white parts of this binary image indicate ROIs (regions of interest) to analyze mean pixel intensity of GS immunoreactivity, proportion of total area, density, and mean area of GS-immunoreactive cells in the m1a region. m1b, myelinated region 1b; m1c, myelinated region 1c; m1cd, myelinated region 1cd; m1d, myelinated region 1d; m2ab, myelinated region 2ab; m2cd, myelinated region 2cd. Scale bar = 200 µm in D for A-C.

FIGURE 5 **A-B:** Images used for quantitative analyses of bisBenzimide (bBM) distribution along the course of the myelinated regions of the normal rat optic nerve. The original image of FIGURE 2D, in which brightness and contrast were not adjusted (in which the brightness levels of an image histogram were not moved or stretched), was modified to create these images. Black background of the original image was removed manually on Adobe Photoshop CS5. The left edges of the m1ab (myelinated region 1ab) and m1a (myelinated region 1a) images indicate the border between the unmyelinated and myelinated regions. The horizontal length of each image is 500 µm in A and 250 µm in B. The background color of each modified image is complete white for the presentation. The

"Retina" and the "OX (optic chiasm)" show the orientation of each modified image. The scale in the bottom of each modified image represents a distance from the border between the unmyelinated and myelinated regions (Distance from u/m Border). **C:** The black binary image used to measure area of the m1a region. **D:** The white parts of this binary image indicate ROIs (regions of interest) to analyze mean pixel intensity of bBM labeling, proportion of total area, density, and mean area of bBM-labeled cell nuclei in the m1a region. m1b, myelinated region 1b; m1c, myelinated region 1c; m1cd, myelinated region 1cd; m1d, myelinated region 1d; m2ab, myelinated region 2ab; m2cd, myelinated region 2cd. Scale bar = 200 μm in D for A-C.

FIGURE 6 **A-B:** Images used for quantitative analyses of myelin basic protein (MBPh[5]) distribution and for those of MBPh-immunoreactive particles along the course of the myelinated regions of the normal rat optic nerve. The original image of FIGURE 2C, in which brightness and contrast were not adjusted (in which the brightness levels of an image histogram were not moved or stretched), was modified to create these images. Black background of the original image was removed manually on Adobe Photoshop CS5. The left

[5] In the companion pater (Kawano, 2025), we used two kinds of anti-myelin basic protein (MBP) antibodies which detect different positions of the MBP protein in order to analyze distribution of the MBP protein in the normal rat optic nerve: One was an antibody reacts with Ala-Ser-Asp-Tyr-Lys-Ser (ASDYKS) in position 131-136 of the classic human myelin basic protein (MBPh), another was an antibody reacts with Asp-Glu-Asn-Pro-Val-Val (DENPVV) in position 82-87 of the full length protein of the cow myelin basic protein (MBPc). Here we describe not MBP but MBPh to clarify which antibody was used to visualize the MBP protein.

edges of the m1ab (myelinated region 1ab) and m1a (myelinated region 1a) images indicate the border between the unmyelinated and myelinated regions. The horizontal length of each image is 500 µm in A and 250 µm in B. The background color of each modified image is complete white for the presentation. The "Retina" and the "OX (optic chiasm)" show the orientation of each modified image. The scale in the bottom of each modified image represents a distance from the border between the unmyelinated and myelinated regions (Distance from u/m Border). **C:** The black binary image used to measure area of the m1a region. **D:** The white parts of this binary image indicate ROIs (regions of interest) to analyze mean pixel intensity of MBPh immunoreactivity, proportion of total area, density, mean area, mean perimeter, and shape descriptors (mean circularity, mean AR (aspect ratio), mean roundness, and mean solidity) of MBPh-immunoreactive particles in the m1a region. m1b, myelinated region 1b; m1c, myelinated region 1c; m1cd, myelinated region 1cd; m1d, myelinated region 1d; m2ab, myelinated region 2ab; m2cd, myelinated region 2cd. Scale bar = 200 µm in D for A-C.

FIGURE 7 Quantitative analysis of glial fibrillary acidic protein (GFAP) distribution along the course of the myelinated regions in the normal rat optic nerve. **A-B** and **D-E**: Mean standardized pixel intensity within each myelinated region of the optic nerve for GFAP immunoreactivity in each region 500 µm in longitudinal length (**A**) and 250 µm in longitudinal length (**D**), and for GFAP immunoreactivity in GFAP-immunoreactive filaments of each region 500 µm in longitudinal length (**B**) and 250 µm in longitudinal length (**E**). Mean pixel intensity values in regions along the nerve were normalized and expressed as a ratio of mean pixel intensity of the myelinated region 1ab (m1ab) value (500 µm) or of the myelinated region 1a (m1a) value (250 µm). **C** and **F**: Standardized proportion of total area of GFAP-immunoreactive filaments within each myelinated region 500 µm in longitudinal

length (**C**) and 250 μm in longitudinal length (**F**). Proportion values in regions along the nerve were normalized and expressed as a ratio of proportion of the m1ab value (500 μm) or of the m1a value (250 μm). Solid circles on the lines of box and whisker plots indicate the intragroup viability for the chemoarchitectural or structural quantitative measures. The upper whisker shows the maximum value, and the lower one represents the minimum value. The thick horizontal line in the box indicates the median. The upper and lower borders of the box show the interquartile range. Open circles represent outliners. The scale in the bottom of each panel indicates a distance from the border between the unmyelinated and myelinated regions (Distance from u/m Border). Note that the intensity of GFAP immunoreactivity was strong in the m1ab region, moderate in myelinated region 1cd (m1cd), and weak in myelinated regions 2ab (m2ab) and 2cd (m2cd). Statistical analyses revealed significant differences in the intensity between the m1ab and m1cd regions, and between the m1cd and m2ab regions. However, there was no significant difference in the intensity between the m2ab and m2cd regions (**A**). In myelinated region 1 (m1), the intensity of GFAP immunoreactivity was the strongest in the m1a region with a gradual decrease in the intensity along the proximal (posterior) course of the optic nerve. Statistical analyses revealed significant differences in the intensity between myelinated regions 1a (m1a) and 1b (m1b), and between myelinated regions 1c (m1c) and 1d (m1d). However, there was no significant difference in the intensity between the m1b and m1c regions (**D**). *Significant difference with $P=0.027 < 0.05$, as determined by the Kruskal-Wallis test with the Steel-Dwass test for multiple comparison. **Significant difference with $P=0.045 < 0.05$, as determined by the method described above.

FIGURE 8 Quantitative analysis of glutamine synthetase (GS) distribution along the course of the myelinated regions in the normal rat optic nerve. **A-B** and **F-G**: Mean standardized pixel intensity within each myelinated region of the optic nerve for GS in each

region 500 µm in longitudinal length (**A**) and 250 µm in longitudinal length (**F**), and for GS in GS-immunoreactive cells of each region 500 µm in longitudinal length (**B**) and 250 µm in longitudinal length (**G**). Mean pixel intensity values in regions along the nerve were normalized and expressed as a ratio of mean pixel intensity of the myelinated region 1ab (m1ab) value (500 µm) or of the myelinated region 1a (m1a) value (250 µm). **C** and **H**: Standardized proportion of total area of GS-immunoreactive cells within each myelinated region 500 µm in longitudinal length (**C**) and 250 µm in longitudinal length (**H**). Proportion values in regions along the nerve were normalized and expressed as a ratio of proportion of the m1ab value (500 µm) or of the m1a value (250 µm). **D** and **I**: Standardized density of GS-immunoreactive cells within each myelinated region 500 µm in longitudinal length (**D**) and 250 µm in longitudinal length (**I**). Density values in regions along the nerve were normalized and expressed as a ratio of density of the m1ab value (500 µm) or of the m1a value (250 µm). **E** and **J**: Mean standardized area of GS-immunoreactive cells within each myelinated region 500 µm in longitudinal length (**E**) and 250 µm in longitudinal length (**J**). Mean area values in regions along the nerve were normalized and expressed as a ratio of mean area of the m1ab value (500 µm) or of the m1a value (250 µm). Solid circles on the lines of box and whisker plots indicate the intragroup viability for the chemoarchitectural or structural quantitative measures. The upper whisker shows the maximum value, and the lower one represents the minimum value. The thick horizontal line in the box indicates the median. The upper and lower borders of the box show the interquartile range. Open circles represent outliners. The scale in the bottom of each panel indicates a distance from the border between the unmyelinated and myelinated regions (Distance from u/m Border). Note that the intensity of GS immunoreactivity was strong in the m1ab region, moderate in the myelinated region 1cd (m1cd), and weak in the myelinated regions 2ab (m2ab) and 2cd (m2cd). Statistical analyses revealed significant differences in the intensity between the m1ab and m1cd regions, and

between the m1cd and m2ab regions. However, there was no significant difference in the intensity between the m2ab and m2cd regions (**A**). In the m1 region, the intensity of GS immunoreactivity was the strongest in the m1a region, moderate in myelinated region 1b (m1b), and the weakest in myelinated regions 1c (m1c) and 1d (m1d). Statistical analyses revealed significant differences in the intensity between the m1a and m1b regions, and between the m1b and m1c regions. However, there was no significant difference in the intensity between the m1c and m1d regions (**F**). *Significant difference with P=0.027 < 0.05, as determined by the Kruskal-Wallis test with the Steel-Dwass test for multiple comparison. **Significant difference with P=0.045 < 0.05, as determined by the method described above.

(The author would like to have the two panels (panels **A-C** (**F-H**) and **D-E** (**I-J**) of FIGURE 8) on opposite pages.)

FIGURE 9 Quantitative analysis of bisBenzimide (bBM; a fluorescent dye for DNA) distribution along the course of the myelinated regions in the normal rat optic nerve. **A-B** and **F-G**: Mean standardized pixel intensity within each myelinated region of the optic nerve for bBM in each region 500 µm in longitudinal length (**A**) and 250 µm in longitudinal length (**F**), and for bBM in bBM-labeled cell nuclei of each region 500 µm in longitudinal length (**B**) and 250 µm in longitudinal length (**G**). Mean pixel intensity values in regions along the nerve were normalized and expressed as a ratio of mean pixel intensity of the myelinated region 1ab (m1ab) value (500 µm) or of the myelinated region 1a (m1a) value (250 µm). **C** and **H**: Standardized proportion of total area of bBM-labeled cell nuclei within each myelinated region 500 µm in longitudinal length (**C**) and 250 µm in longitudinal length (**H**). Proportion values in regions along the nerve were normalized and expressed as a ratio of proportion of the m1ab value (500 µm) or of the m1a value (250 µm). **D** and **I**: Standardized density of bBM-labeled cell nuclei within each myelinated region 500 µm in longitudinal

length (**D**) and 250 µm in longitudinal length (**I**). Density values in regions along the nerve were normalized and expressed as a ratio of density of the m1ab value (500 µm) or of the m1a value (250 µm). **E** and **J**: Mean standardized area of bBM-labeled cell nuclei within each myelinated region 500 µm in longitudinal length (**E**) and 250 µm in longitudinal length (**J**). Mean area values in regions along the nerve were normalized and expressed as a ratio of mean area of the m1ab value (500 µm) or of the m1a value (250 µm). Solid circles on the lines of box and whisker plots indicate the intragroup viability for the chemoarchitectural or structural quantitative measures. The upper whisker shows the maximum value, and the lower one represents the minimum value. The thick horizontal line in the box indicates the median. The upper and lower borders of the box show the interquartile range. Open circles represent outliners. The scale in the bottom of each panel indicates a distance from the border between the unmyelinated and myelinated regions (Distance from u/m Border). Note that the intensity of bBM labeling was strong in the m1ab region, and moderate in myelinated regions 1cd (m1cd), 2ab (m2ab), and 2cd (m2cd). Statistical analyses revealed significant differences in the intensity between the m1ab and m1cd regions, between the m1ab and m2ab regions, and between the m1ab and m2cd regions. However, there was no significant difference among the m1cd, m2ab, and m2cd regions (**A**). In myelinated region 1 (m1), the intensity of bBM labeling was strong in the m1a region, strong-to-moderate in myelinated region 1b (m1b), and moderate in myelinated regions 1c (m1c) and 1d (m1d). Statistical analyses revealed significant differences in the intensity between the m1a and m1c regions, and between the m1a and m1d regions. However, there was no significant difference in the intensity between the m1a and m1b regions, between the m1b and m1c regions, and between the m1c and m1d regions (**F**). *Significant difference with $P=0.027 < 0.05$, as determined by the Kruskal-Wallis test with the Steel-Dwass test for multiple comparison.

(The author would like to have the two panels (panels **A-C** (**F-H**) and **D-E** (**I-J**) of FIGURE 9) on opposite pages.)

FIGURE 10 Quantitative analysis of myelin basic protein (MBPh[6]) distribution along the course of the myelinated regions in the normal rat optic nerve. **A-B** and **G-H**: Mean standardized pixel intensity within each myelinated region of the optic nerve for MBPh in each region 500 μm in longitudinal length (**A**) and 250 μm in longitudinal length (**G**), and for MBPh in MBPh-immunoreactive particles of each region 500 μm in longitudinal length (**B**) and 250 μm in longitudinal length (**H**). Mean pixel intensity values in regions along the nerve were normalized and expressed as a ratio of mean pixel intensity of the myelinated region 1ab (m1ab) value (500 μm) or of the myelinated region 1a (m1a) value (250 μm). **C** and **I**: Standardized proportion of total area of MBPh-immunoreactive particles within each myelinated region 500 μm in longitudinal length (**C**) and 250 μm in longitudinal length (**I**). Proportion values in regions along the nerve were normalized and expressed as a ratio of proportion of the m1ab value (500 μm) or of the m1a value (250 μm). **D** and **J**: Standardized density of MBPh-immunoreactive particles within each myelinated region 500 μm in

[6] In the companion pater (Kawano, 2025), we used two kinds of anti-myelin basic protein (MBP) antibodies which detect different positions of the MBP protein in order to analyze distribution of the MBP protein in the normal rat optic nerve: One was an antibody reacts with Ala-Ser-Asp-Tyr-Lys-Ser (ASDYKS) in position 131-136 of the classic human myelin basic protein (MBPh), another was an antibody reacts with Asp-Glu-Asn-Pro-Val-Val (DENPVV) in position 82-87 of the full length protein of the cow myelin basic protein (MBPc). Here we describe not MBP but MBPh to clarify which antibody was used to visualize the MBP protein.

longitudinal length (**D**) and 250 μm in longitudinal length (**J**). Density values in regions along the nerve were normalized and expressed as a ratio of density of the m1ab value (500 μm) or of the m1a value (250 μm). **E** and **K**: Mean standardized area of MBPh-immunoreactive particles within each myelinated region 500 μm in longitudinal length (**E**) and 250 μm in longitudinal length (**K**). Mean area values in regions along the nerve were normalized and expressed as a ratio of mean area of the m1ab value (500 μm) or of the m1a value (250 μm). **F** and **L**: Mean standardized perimeter of MBPh-immunoreactive particles within each myelinated region 500 μm in longitudinal length (**F**) and 250 μm in longitudinal length (**L**). Mean perimeter values in regions along the nerve were normalized and expressed as a ratio of mean perimeter of the m1ab value (500 μm) or of the m1a value (250 μm). Solid circles on the lines of box and whisker plots indicate the intragroup viability for the chemoarchitectural or structural quantitative measures. The upper whisker shows the maximum value, and the lower one represents the minimum value. The thick horizontal line in the box indicates the median. The upper and lower borders of the box show the interquartile range. Open circles represent outliners. The scale in the bottom of each panel indicates a distance from the border between the unmyelinated and myelinated regions (Distance from u/m Border). Note that the intensity of MBPh immunoreactivity in MBPh-immunoreactive particles was strong in the m1ab region, strong-to-moderate in myelinated region 1cd (m1cd), and moderate in myelinated regions 2ab (m2ab) and 2cd (m2cd). Statistical analyses revealed significant differences in the intensity between the m1ab and m2ab regions, and between the m1ab and m2cd regions. However, there was no significant difference in the intensity between the m1ab and m1cd regions, between the m1cd and m2ab regions, and between the m2ab and m2cd regions (**B**). In myelinated region 1 (m1), the intensity of MBPh immunoreactivity in the MBPh-immunoreactive particles was strong in the m1a region, strong-to-moderate in myelinated region 1c (m1c), moderate in myelinated

regions 1b (m1b) and 1d (m1d). Statistical analyses revealed significant differences in the intensity of immunoreactivity between the m1a and m1b regions, and between the m1a and m1d regions. However, there was no significant difference in the intensity between the m1a and m1c regions, between the m1b and m1c region, and between the m1c and m1d regions (**H**). The mean area was large in the m1ab region, but small in the m1cd, m2ab, and m2cd regions. Statistical analyses revealed significant differences in the mean area between the m1ab and m1cd regions, and between the m1ab and m2ab regions. However, there was no significant difference in the mean area between the m1ab and m2cd regions (**E**). In the m1 region, the mean area was large in the m1a region, but small in the m1b, m1c, and m1d regions. Statistical analyses revealed significant differences in the mean area between the m1a and m1b regions, between m1a and m1c regions, and between the m1a and m1d regions. However, there was no significant difference in the mean area among the m1b, m1c, and m1d regions (**K**). *Significant difference with $P=0.027 < 0.05$, as determined by the Kruskal-Wallis test with the Steel-Dwass test for multiple comparison.

(The author would like to have the two panels (panels **A-C** (**G-I**) and **D-F** (**J-L**) of FIGURE 10) on opposite pages.)

FIGURE 11 Quantitative analysis of shape descriptors of myelin basic protein (MBPh[7])-immunoreactive particles along the course of the myelinated regions in the normal

[7] In the companion pater (Kawano, 2025), we used two kinds of anti-myelin basic protein (MBP) antibodies which detect different positions of the MBP protein in order to analyze distribution of the MBP protein in the normal rat optic nerve: One was an antibody reacts with Ala-Ser-Asp-Tyr-Lys-Ser (ASDYKS) in position 131-136 of the classic human myelin basic protein (MBPh), another was an antibody reacts with Asp-Glu-Asn-Pro-Val-Val

rat optic nerve. **A** and **E**: Mean standardized circularity of MBPh-immunoreactive particles within each myelinated region 500 µm in longitudinal length (**A**) and 250 µm in longitudinal length (**E**). Mean circularity values in regions along the nerve were normalized and expressed as a ratio of mean circularity of the myelinated region 1ab (m1ab) value (500 µm) or of the myelinated region 1a (m1a) value (250 µm). **B** and **F**: Mean standardized AR (aspect ratio) of MBPh-immunoreactive particles within each myelinated region 500 µm in longitudinal length (**B**) and 250 µm in longitudinal length (**F**). Mean AR values in regions along the nerve were normalized and expressed as a ratio of mean AR of the m1ab value (500 µm) or of the m1a value (250 µm). **C** and **G**: Mean standardized roundness of MBPh-immunoreactive particles within each myelinated region 500 µm in longitudinal length (**C**) and 250 µm in longitudinal length (**G**). Mean roundness values in regions along the nerve were normalized and expressed as a ratio of mean roundness of the m1ab value (500 µm) or of the m1a value (250 µm). **D** and **H**: Mean standardized solidity of MBPh-immunoreactive particles within each myelinated region 500 µm in longitudinal length (**D**) and 250 µm in longitudinal length (**H**). Mean solidity values in regions along the nerve were normalized and expressed as a ratio of mean solidity of the m1ab value (500 µm) or of the m1a value (250 µm). Solid circles on the lines of box and whisker plots indicate the intragroup viability for the structural quantitative measures. The upper whisker shows the maximum value, and the lower one represents the minimum value. The thick horizontal line in the box indicates the median. The upper and lower borders of the box show the interquartile range. Open circles represent outliners. The scale in the bottom of each panel indicates a distance from the border between

---

(DENPVV) in position 82-87 of the full length protein of the cow myelin basic protein (MBPc). Here we describe not MBP but MBPh to clarify which antibody was used to visualize the MBP protein.

the unmyelinated and myelinated regions (Distance from u/m Border). Note that the mean circularity was medium in the m1ab region, large in myelinated region 1cd (m1cd), and small-to-large in myelinated regions 2ab (m2ab) and 2cd (m2cd). Statistical analyses revealed significant difference in the mean circularity between the m1ab and m1cd regions. However, there was no significant difference in the mean circularity among the m1cd, m2ab, and m2cd regions (**A**). In myelinated region 1 (m1), the mean circularity was medium in the m1a region, medium-to-large in myelinated regions 1b (m1b) and 1c (m1c), and large in myelinated region 1d (m1d). Statistical analyses revealed significant difference in the mean circularity between the m1a and m1d regions. However, there was no significant difference in the mean circularity between the m1a and m1b region, between the m1b and m1c region, and between the m1c and m1d regions (**E**). *Significant difference with $P=0.027 < 0.05$, as determined by the Kruskal-Wallis test with the Steel-Dwass test for multiple comparison.

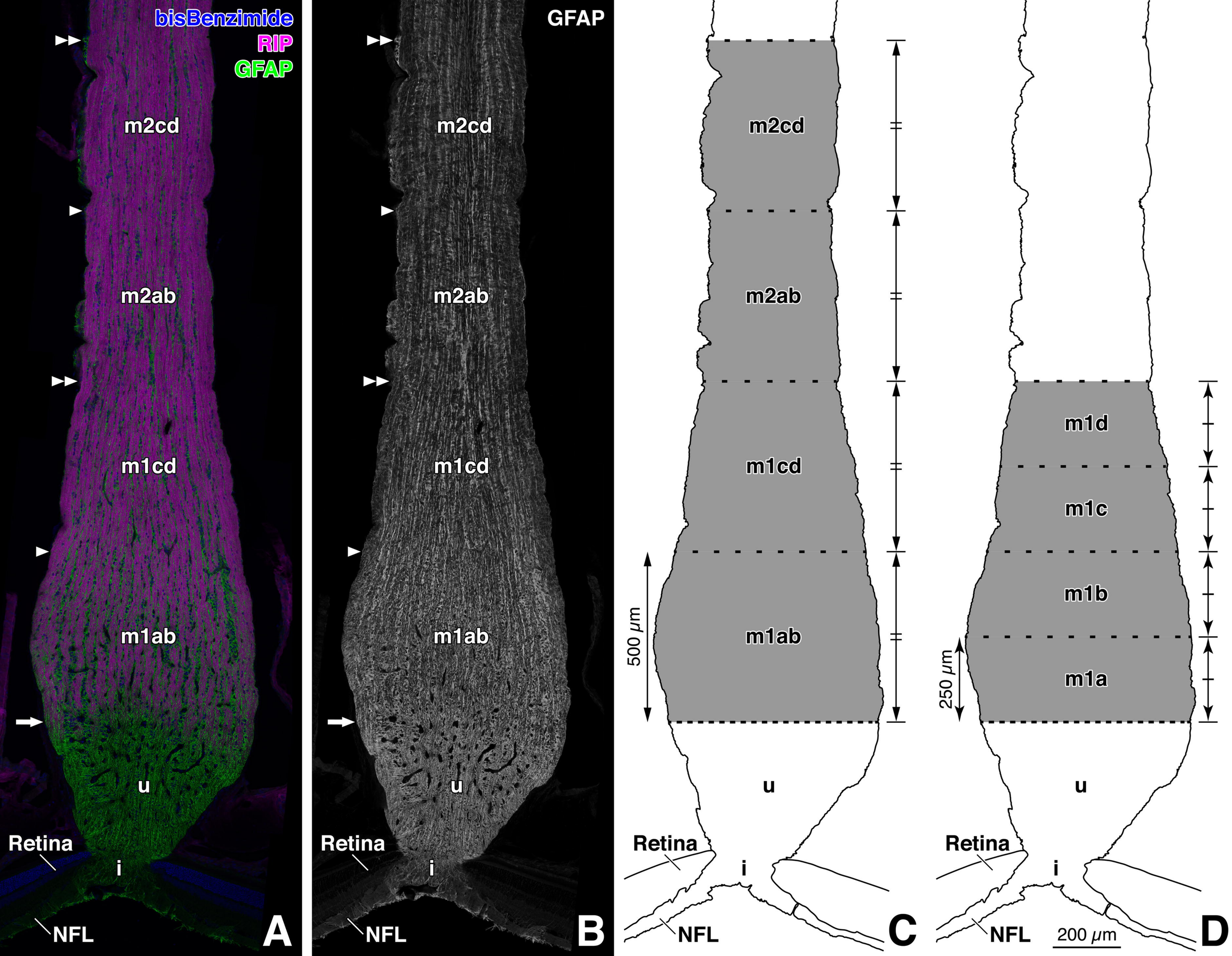
bisBenzimide
RIP
GFAP
m2cd
m2ab
m1cd
m1ab
u
Retina
i
NFL
A
GFAP
m2cd
m2ab
m1cd
m1ab
u
Retina
i
NFL
B
m2cd
m2ab
m1cd
m1ab
500 μm
u
Retina
i
NFL
C
m1d
m1c
m1b
m1a
250 μm
u
Retina
i
NFL
200 μm
D

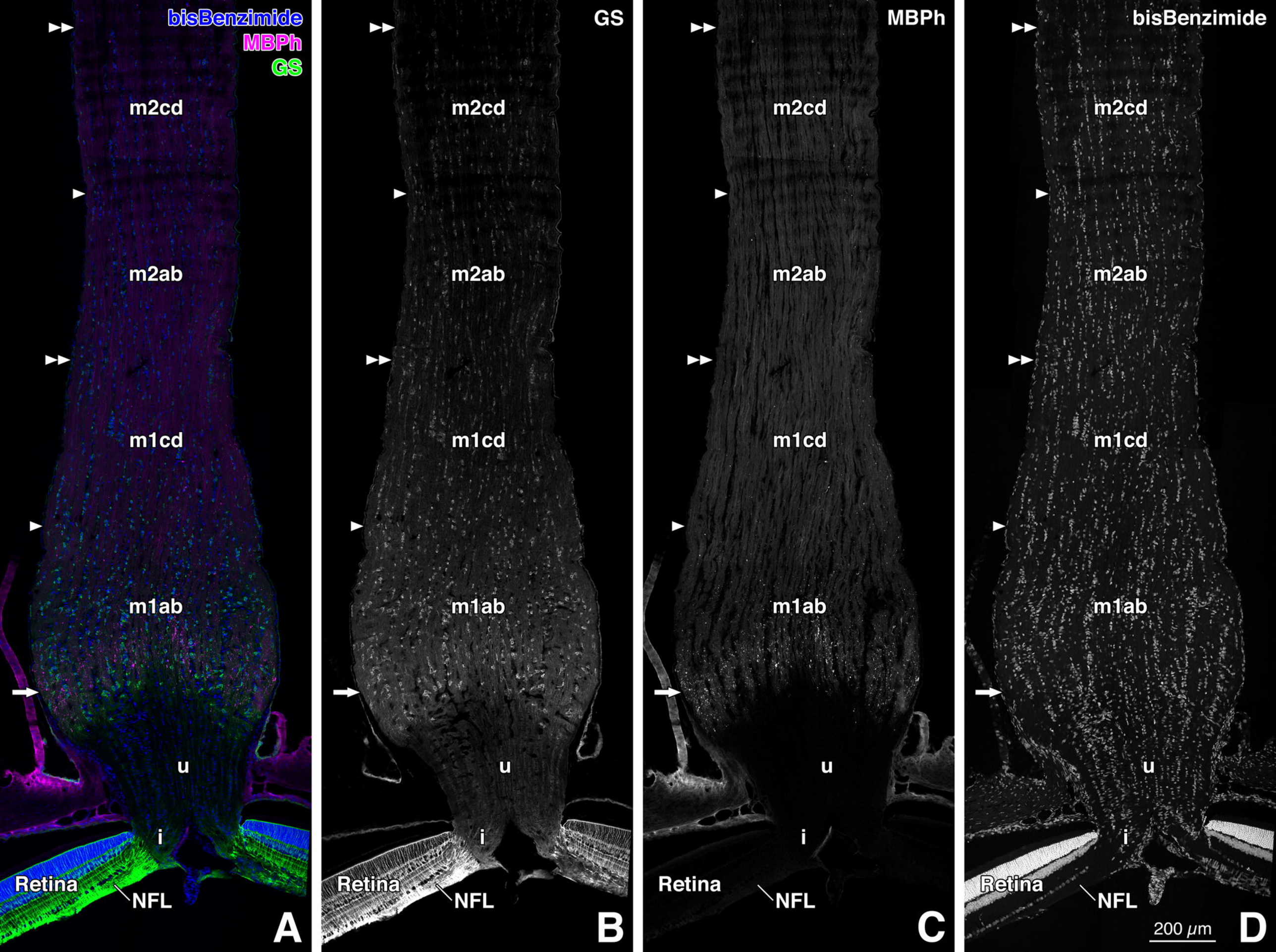
bisBenzimide
MBPh
GS
m2cd
m2ab
m1cd
m1ab
u
i
Retina
NFL
A
GS
B
MBPh
C
bisBenzimide
200 μm
D

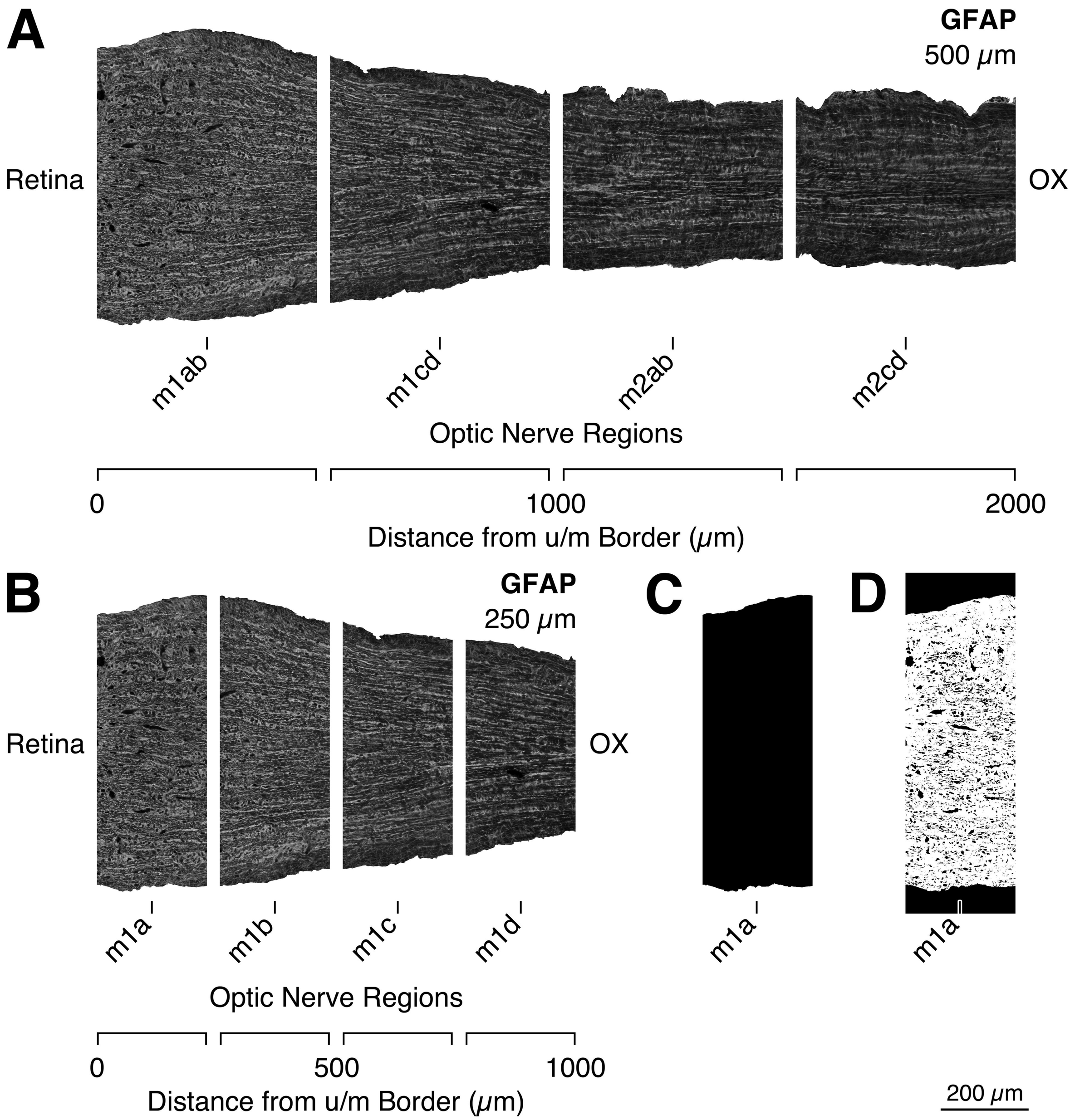
A
GFAP
500 μm
Retina
OX
m1ab
m1cd
m2ab
m2cd
Optic Nerve Regions
0
1000
2000
Distance from u/m Border (μm)
B
GFAP
250 μm
Retina
OX
m1a
m1b
m1c
m1d
Optic Nerve Regions
0
500
1000
Distance from u/m Border (μm)
C
m1a
D
m1a
200 μm

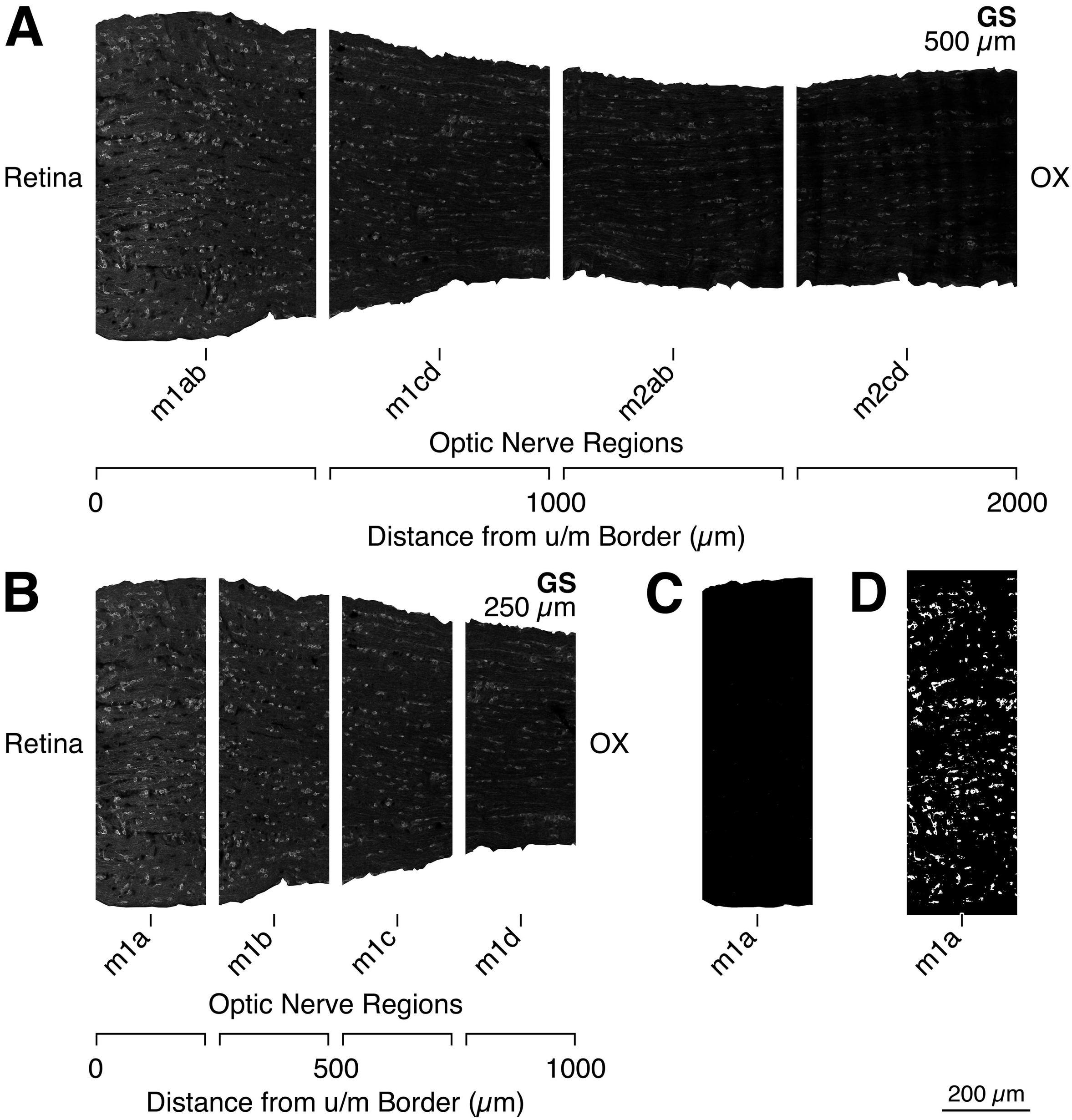
A
GS
500 μm
Retina
OX
m1ab
m1cd
m2ab
m2cd
Optic Nerve Regions
0
1000
2000
Distance from u/m Border (μm)
B
GS
250 μm
Retina
OX
m1a
m1b
m1c
m1d
Optic Nerve Regions
0
500
1000
Distance from u/m Border (μm)
C
m1a
D
m1a
200 μm

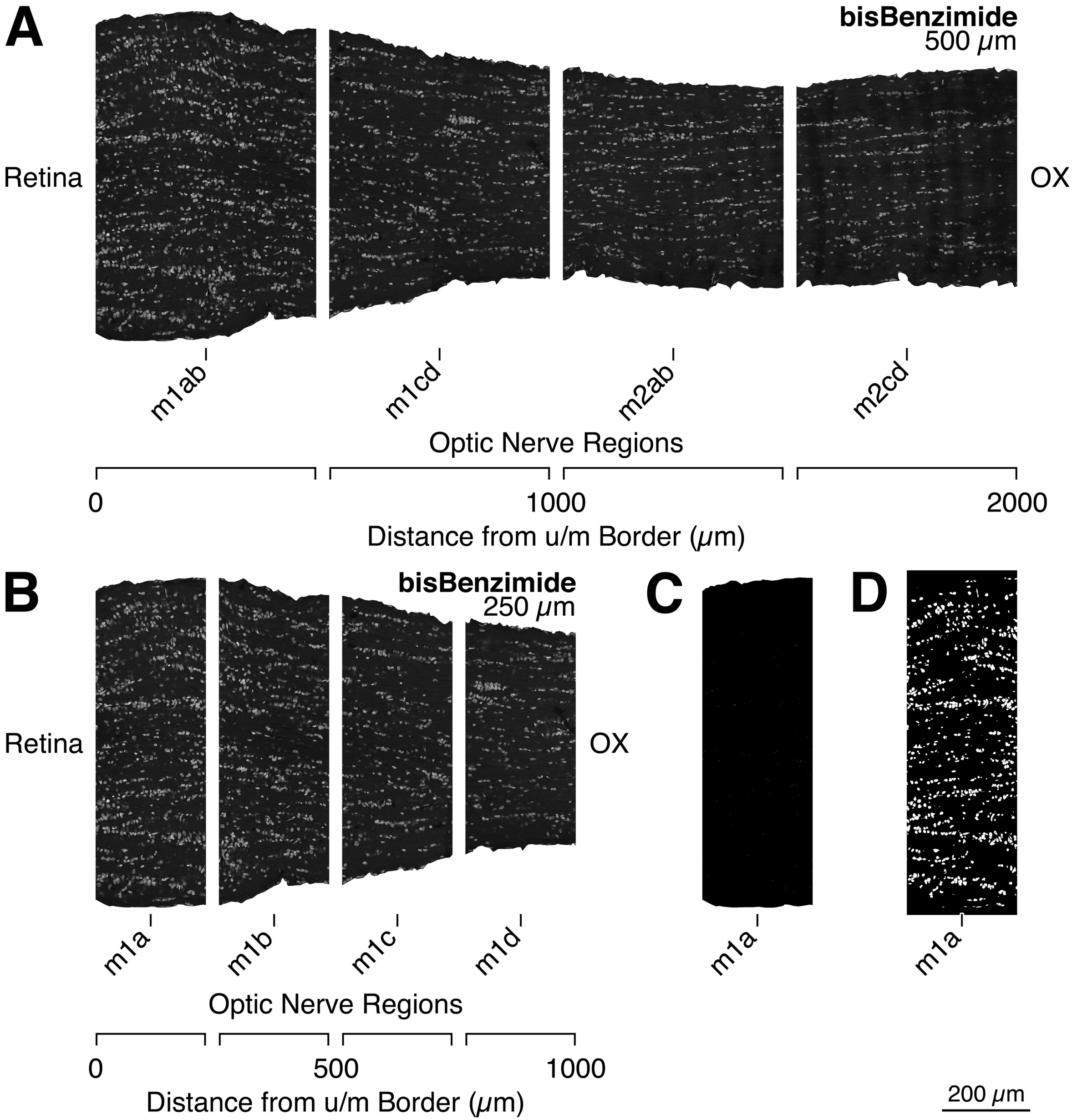
A
bisBenzimide
500 μm
Retina
OX
m1ab
m1cd
m2ab
m2cd
Optic Nerve Regions
0
1000
2000
Distance from u/m Border (μm)
B
bisBenzimide
250 μm
Retina
OX
m1a
m1b
m1c
m1d
Optic Nerve Regions
0
500
1000
Distance from u/m Border (μm)
C
m1a
D
m1a
200 μm

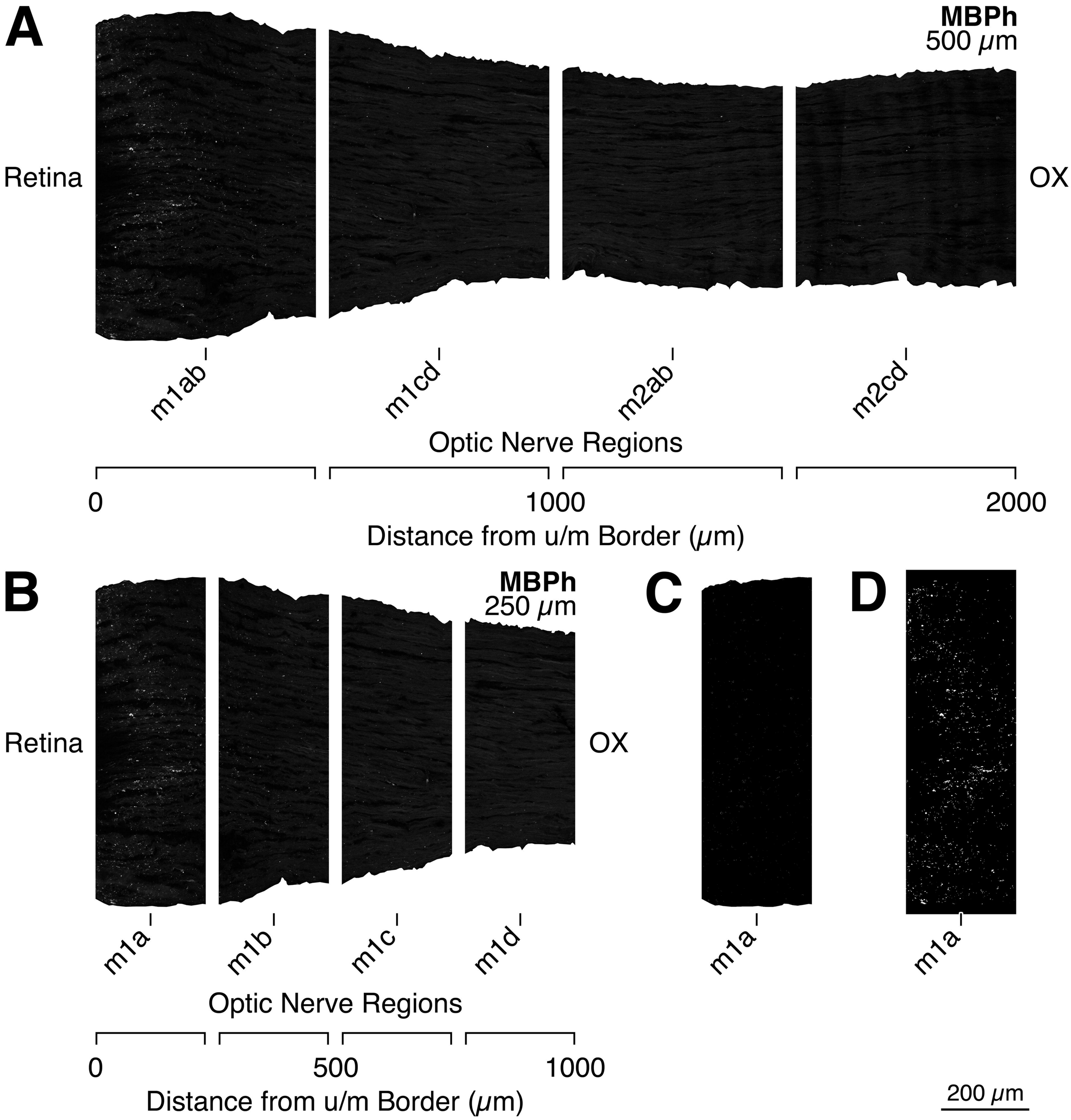
A
MBPh
500 μm
Retina
OX
m1ab
m1cd
m2ab
m2cd
Optic Nerve Regions
0
1000
2000
Distance from u/m Border (μm)
B
MBPh
250 μm
Retina
OX
m1a
m1b
m1c
m1d
Optic Nerve Regions
0
500
1000
Distance from u/m Border (μm)
C
m1a
D
m1a
200 μm

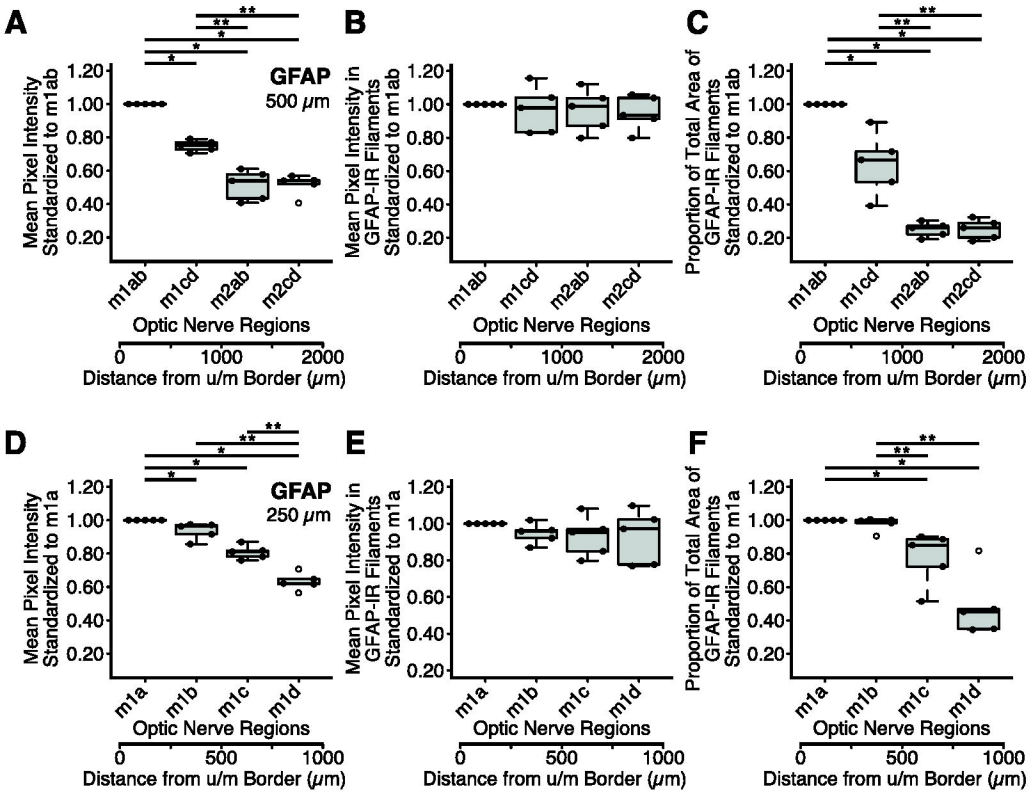
A
B
C
D
E
F
GFAP
500 μm
GFAP
250 μm
Mean Pixel Intensity Standardized to m1ab
Mean Pixel Intensity in GFAP-IR Filaments Standardized to m1ab
Proportion of Total Area of GFAP-IR Filaments Standardized to m1ab
Mean Pixel Intensity Standardized to m1a
Mean Pixel Intensity in GFAP-IR Filaments Standardized to m1a
Proportion of Total Area of GFAP-IR Filaments Standardized to m1a
1.20
1.00
0.80
0.60
0.40
0.20
m1ab
m1cd
m2ab
m2cd
m1a
m1b
m1c
m1d
Optic Nerve Regions
0
1000
2000
500
Distance from u/m Border (μm)
*
**

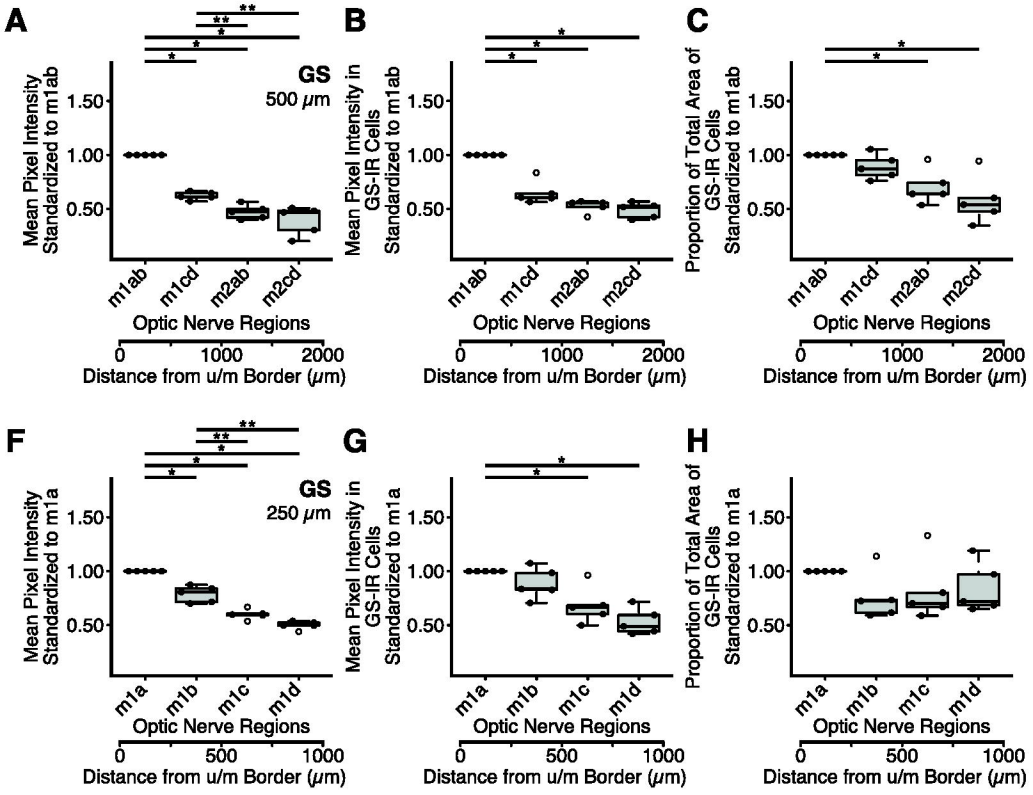
A
B
C
F
G
H
GS
500 μm
250 μm
Mean Pixel Intensity Standardized to m1ab
Mean Pixel Intensity in GS-IR Cells Standardized to m1ab
Proportion of Total Area of GS-IR Cells Standardized to m1ab
Mean Pixel Intensity Standardized to m1a
Mean Pixel Intensity in GS-IR Cells Standardized to m1a
Proportion of Total Area of GS-IR Cells Standardized to m1a
1.50
1.00
0.50
m1ab
m1cd
m2ab
m2cd
m1a
m1b
m1c
m1d
Optic Nerve Regions
0
1000
2000
500
Distance from u/m Border (μm)
*
**

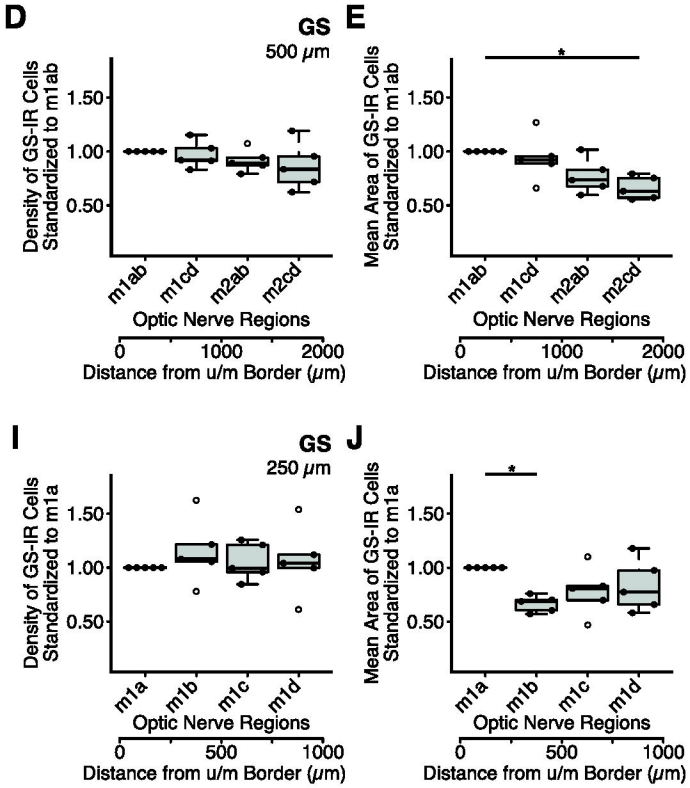
D
GS
500 μm
Density of GS-IR Cells
Standardized to m1ab
1.50
1.00
0.50
m1ab
m1cd
m2ab
m2cd
Optic Nerve Regions
0
1000
2000
Distance from u/m Border (μm)
E
*
Mean Area of GS-IR Cells
Standardized to m1ab
1.50
1.00
0.50
m1ab
m1cd
m2ab
m2cd
Optic Nerve Regions
0
1000
2000
Distance from u/m Border (μm)
I
GS
250 μm
Density of GS-IR Cells
Standardized to m1a
1.50
1.00
0.50
m1a
m1b
m1c
m1d
Optic Nerve Regions
0
500
1000
Distance from u/m Border (μm)
J
*
Mean Area of GS-IR Cells
Standardized to m1a
1.50
1.00
0.50
m1a
m1b
m1c
m1d
Optic Nerve Regions
0
500
1000
Distance from u/m Border (μm)

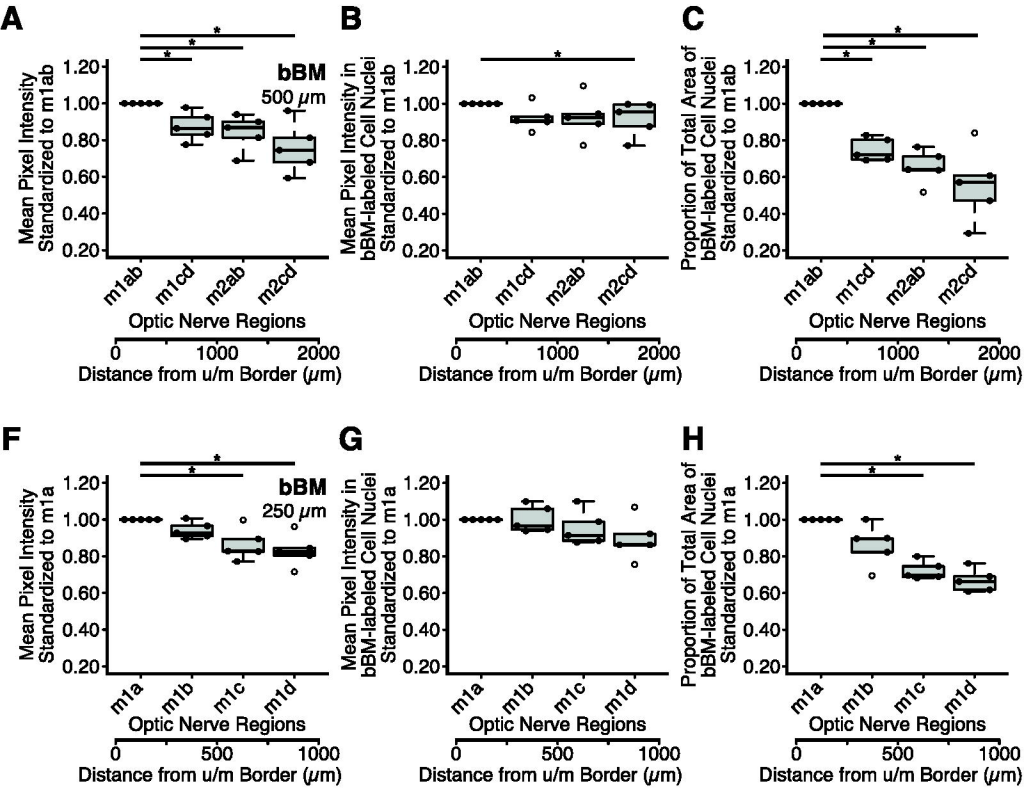
A
B
C
F
G
H
bBM
500 μm
250 μm
Mean Pixel Intensity Standardized to m1ab
Mean Pixel Intensity in bBM-labeled Cell Nuclei Standardized to m1ab
Proportion of Total Area of bBM-labeled Cell Nuclei Standardized to m1ab
Mean Pixel Intensity Standardized to m1a
Mean Pixel Intensity in bBM-labeled Cell Nuclei Standardized to m1a
Proportion of Total Area of bBM-labeled Cell Nuclei Standardized to m1a
1.20
1.00
0.80
0.60
0.40
0.20
m1ab
m1cd
m2ab
m2cd
m1a
m1b
m1c
m1d
Optic Nerve Regions
0
1000
2000
500
Distance from u/m Border (μm)
*

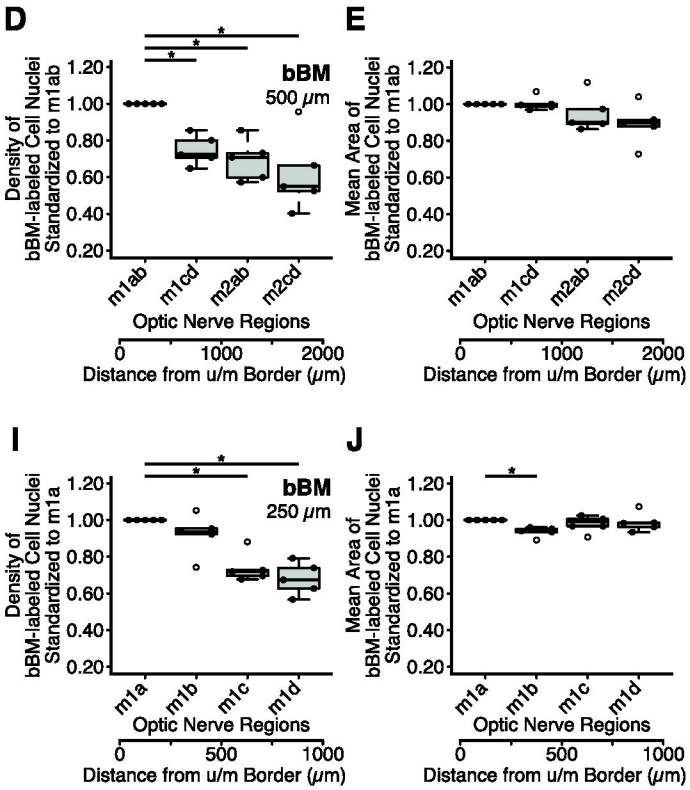
D
E
I
J
bBM
500 μm
bBM
250 μm
Density of
bBM-labeled Cell Nuclei
Standardized to m1ab
Density of
bBM-labeled Cell Nuclei
Standardized to m1a
Mean Area of
bBM-labeled Cell Nuclei
Standardized to m1ab
Mean Area of
bBM-labeled Cell Nuclei
Standardized to m1a
1.20
1.00
0.80
0.60
0.40
0.20
m1ab
m1cd
m2ab
m2cd
m1a
m1b
m1c
m1d
Optic Nerve Regions
0
1000
2000
500
Distance from u/m Border (μm)
*

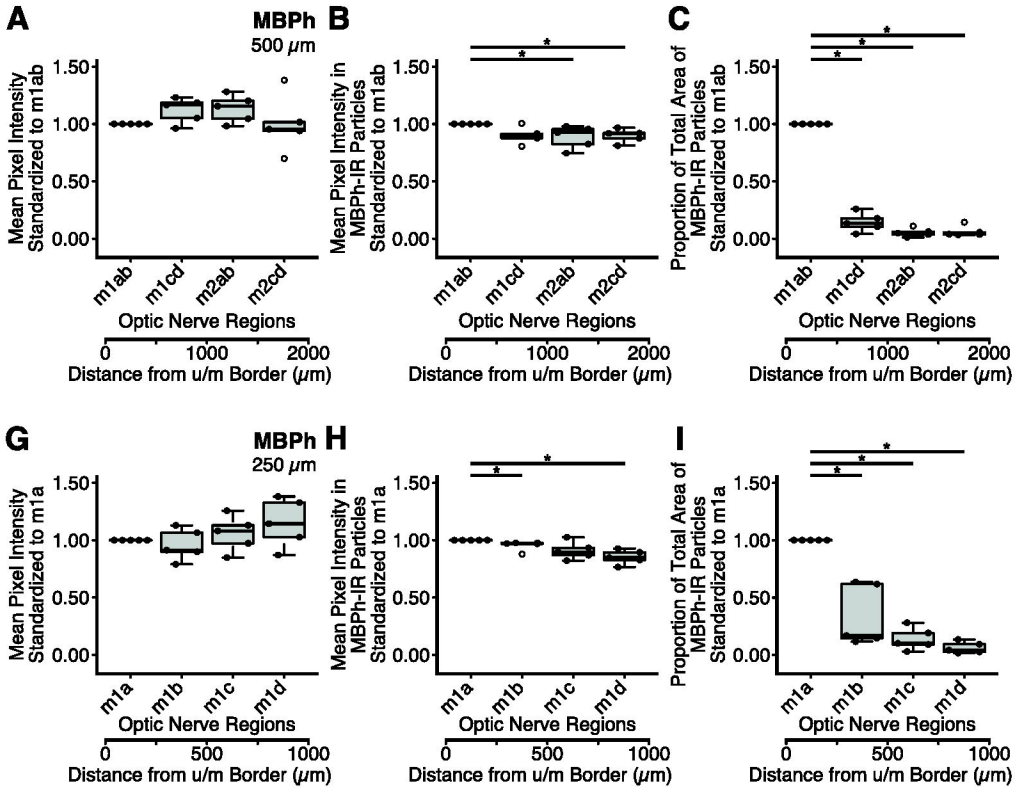
A
MBPh
500 μm
Mean Pixel Intensity Standardized to m1ab
1.50
1.00
0.50
0.00
m1ab
m1cd
m2ab
m2cd
Optic Nerve Regions
0
1000
2000
Distance from u/m Border (μm)
B
Mean Pixel Intensity in MBPh-IR Particles Standardized to m1ab
*
*
C
Proportion of Total Area of MBPh-IR Particles Standardized to m1ab
*
*
*
G
MBPh
250 μm
Mean Pixel Intensity Standardized to m1a
m1a
m1b
m1c
m1d
500
1000
H
Mean Pixel Intensity in MBPh-IR Particles Standardized to m1a
I
Proportion of Total Area of MBPh-IR Particles Standardized to m1a

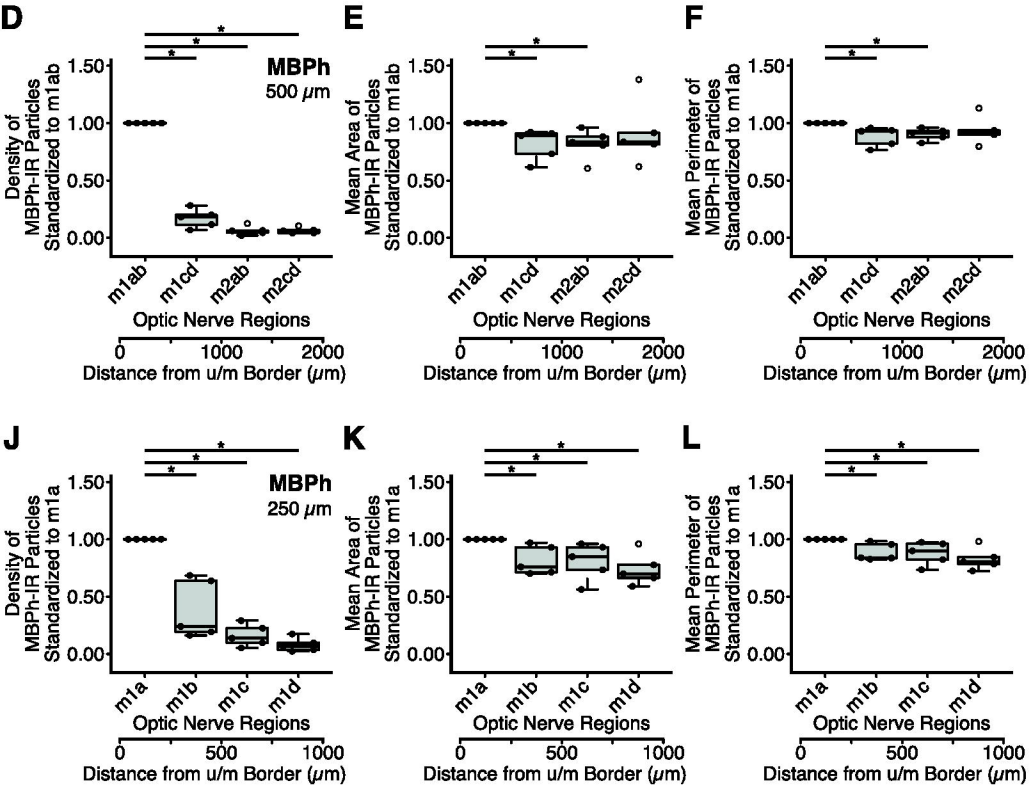
D
E
F
J
K
L
MBPh
500 μm
MBPh
250 μm
Density of MBPh-IR Particles Standardized to m1ab
Mean Area of MBPh-IR Particles Standardized to m1ab
Mean Perimeter of MBPh-IR Particles Standardized to m1ab
Density of MBPh-IR Particles Standardized to m1a
Mean Area of MBPh-IR Particles Standardized to m1a
Mean Perimeter of MBPh-IR Particles Standardized to m1a
1.50
1.00
0.50
0.00
m1ab
m1cd
m2ab
m2cd
m1a
m1b
m1c
m1d
Optic Nerve Regions
0
1000
2000
500
Distance from u/m Border (μm)
*

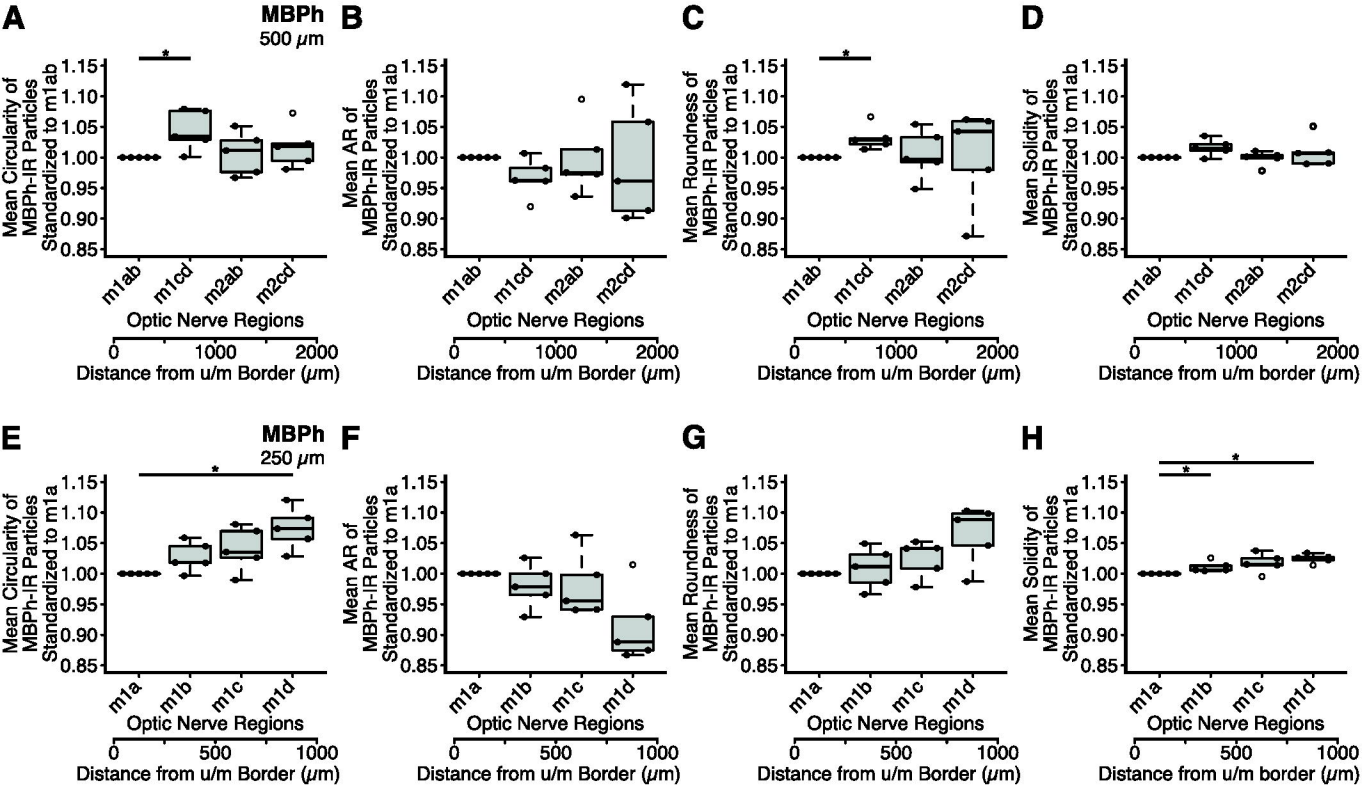
A
MBPh
500 μm
Mean Circularity of MBPh-IR Particles Standardized to m1ab
B
Mean AR of MBPh-IR Particles Standardized to m1ab
C
Mean Roundness of MBPh-IR Particles Standardized to m1ab
D
Mean Solidity of MBPh-IR Particles Standardized to m1ab
E
MBPh
250 μm
Mean Circularity of MBPh-IR Particles Standardized to m1a
F
Mean AR of MBPh-IR Particles Standardized to m1a
G
Mean Roundness of MBPh-IR Particles Standardized to m1a
H
Mean Solidity of MBPh-IR Particles Standardized to m1a
1.15
1.10
1.05
1.00
0.95
0.90
0.85
*
m1ab
m1cd
m2ab
m2cd
m1a
m1b
m1c
m1d
Optic Nerve Regions
0
1000
2000
500
Distance from u/m Border (μm)
Distance from u/m border (μm)

TABLE 1. Primary antibodies used in this study.

Antigen	Immunogen	Manufacturer, cat. no., (lot no.)	Host, RRID	Dilution
Glial fibrillary acidic protein (GFAP)	Purified bovine GFAP	Chemicon (Temecula, CA), AB5804, (0604027868)	Rb; polyclonal, RRID: AB_2109645	1:500
Glutamine synthetase (GS)	A synthetic peptide corresponding to the C-terminus of mouse glutamine synthetase (amino acids 357-373 with N-terminally added lysine) conjugated to KLH	Sigma-Aldrich (Saint Louis, MO), G2781, (115K4794)	Rb; polyclonal, RRID: AB_259853	1:5,000
GS	Sheep glutamine synthetase (1-373: Full Length)	BD Biosciences (San Diego, CA), Pharmingen, 610517, (01915)	Ms; monoclonal, RRID: AB_397879	1:500
Myelin basic protein, human (MBPh) [SMI-99]	Human myelin basic protein peptide containing amino acids 131-136 (-Ala-Ser-Asp-Tyr-Lys-Ser-)	Covance (Princeton, NJ), SMI-99P, (E12DF00768)	Ms; monoclonal, RRID: AB_10120129	1:1,000
Neurofilament H non-phosphorylated [SMI-32]	Fischer 344 rat hypothalamus	Covance, SMI-32R, (E11CF00693)	Ms; monoclonal, RRID: AB_509997	1:250
Oligodendrocytes [RIP]	Rat olfactory bulb	Chemicon, MAB1580, (25040064)	Ms; monoclonal, RRID: AB_94266	1:20,000

Abbreviations: Ms, mouse; Rb, rabbit.